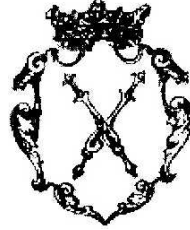


JAGIELLONIAN UNIVERSITY  
INSTITUTE of PHYSICS



Determination of the total width of the  $\eta'$  meson

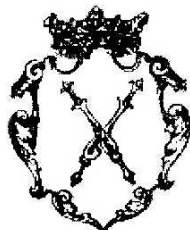
Eryk Mirosław Czerwiński

PhD thesis prepared in the Department of Nuclear Physics  
of the Jagiellonian University and in the Institute  
of Nuclear Physics of the Research Center Jülich  
under supervision of Prof. Paweł Moskal

Cracow 2009



UNIwersYTET JAGIELLOŃSKI  
INSTYTUT FIZYKI



Wyznaczenie szerokości całkowitej mezonu  $\eta'$

Eryk Mirosław Czerwiński

Praca doktorska wykonana w Zakładzie Fizyki Jądrowej  
Uniwersytetu Jagiellońskiego oraz w Instytucie Fizyki  
Jądrowej w Centrum Badawczym w Jülich pod kierunkiem  
dr. hab. Pawła Moskala, prof. UJ

Kraków 2009



*The reasonable man adapts himself to the world;  
the unreasonable one persists in trying to adapt the world to himself.  
Therefore all progress depends on the unreasonable man.*

George Bernard Shaw



## Abstract

The aim of this work was to determine the total width of the  $\eta'$  meson. The investigated meson was produced via the  $pp \rightarrow pp\eta'$  reaction in the collisions of beam protons from COSY synchrotron with protons from a hydrogen cluster target. The COSY-11 detector was used for the measurement of the four-momentum vectors of outgoing protons. The mass of unregistered meson was determined via the missing mass technique, while the total width was directly derived from the mass distributions established at five different beam momenta. Parallel monitoring of the crucial parameters (e.g. size and position of the target stream) and the measurement close-to-threshold permitted to obtain mass resolution of  $\text{FWHM} = 0.33 \text{ MeV}/c^2$ .

Based on the sample of more than 2300 reconstructed  $pp \rightarrow pp\eta'$  events the determined total width of the  $\eta'$  meson amounts to  $\Gamma_{\eta'} = 0.226 \pm 0.017(\text{stat.}) \pm 0.014(\text{syst.}) \text{ MeV}$ , which is the most precise measurement until now.





## Streszczenie

Celem tej pracy było wyznaczenie szerokości całkowitej mezonu  $\eta'$ . Badany mezon był produkowany w reakcji  $pp \rightarrow pp\eta'$  w zderzeniach protonów wiązki synchrotronu COSY oraz protonów z wodorowej tarczy klastrowej. Do pomiaru czteropędów wylatujących protonów użyty został detektor COSY-11. Masa nierejestrowanego mezonu była wyznaczona dzięki metodzie masy brakującej, podczas gdy całkowita szerokość została otrzymana bezpośrednio z widm masy brakującej uzyskanych dla pięciu różnych pędów wiązki. Równoczesne monitorowanie kluczowych parametrów (np. takich jak rozmiar i pozycja strumienia tarczy) oraz wykonanie pomiaru w pobliżu progu kinematycznego na produkcję mezonu  $\eta'$  pozwoliło otrzymać dokładność wyznaczenia masy równą  $\text{FWHM} = 0.33 \text{ MeV}/c^2$ .

W oparciu o ponad 2300 zrekonstruowanych zdarzeń  $pp \rightarrow pp\eta'$  wyznaczona szerokość całkowita mezonu  $\eta'$  wynosi  $\Gamma_{\eta'} = 0.226 \pm 0.017(\text{stat.}) \pm 0.014(\text{syst.}) \text{ MeV}$ , co jest najdokładniejszym dotychczas wynikiem pomiaru tej wielkości.



# Contents

<b>1</b>	<b>Introduction</b>	<b>1</b>
<b>2</b>	<b>Motivation for the determination of the total width of the <math>\eta'</math> meson</b>	<b>3</b>
<b>3</b>	<b>Principle of the measurement – simplicity is beautiful</b>	<b>7</b>
3.1	COoler SYnchrotron COSY . . . . .	8
3.2	Cluster target . . . . .	10
3.3	COSY–11 detector setup . . . . .	12
<b>4</b>	<b>First steps on the way to the total width</b>	<b>17</b>
4.1	Preselection of data . . . . .	17
4.2	Calibration of detectors . . . . .	19
4.2.1	Drift chambers . . . . .	19
4.2.1.1	Relative time offsets of wires . . . . .	19
4.2.1.2	Time-space calibration . . . . .	20
4.2.1.3	Relative positions of the drift chambers . . . . .	22
4.2.2	Timing of scintillator detectors . . . . .	23
4.3	Properties of the cluster target stream . . . . .	24
4.3.1	Diagnosis unit – wire device . . . . .	25
4.3.2	Kinematic ellipse from $pp \rightarrow pp$ events . . . . .	28
4.3.3	Density distribution of the cluster target stream . . . . .	32
4.4	Monitoring of the stability of the proton beam . . . . .	34
4.4.1	Synchrotron parameters . . . . .	34
4.4.2	Atmospheric conditions . . . . .	36
<b>5</b>	<b>Identification of the <math>pp \rightarrow pp\eta'</math> reaction</b>	<b>37</b>
5.1	Identification of the outgoing protons . . . . .	37
5.2	Determination of the relative beam momenta . . . . .	38
5.3	Missing mass spectra and background subtraction . . . . .	38
5.3.1	Experimental background from different energies . . . . .	38
5.3.2	Background parametrisation with polynomial fit . . . . .	40

5.4	Absolute beam momentum determination . . . . .	42
<b>6</b>	<b>Determination of the total width</b>	<b>45</b>
6.1	Comparison of experimental data with simulations . . . . .	45
6.2	Systematic error estimation . . . . .	49
<b>7</b>	<b>Summary</b>	<b>51</b>
	<b>Acknowledgments</b>	<b>55</b>
	<b>Bibliography</b>	<b>57</b>

# Chapter 1

## Introduction

Enlarging the knowledge about nature can be realised either by taking into account a larger field for investigations or by focusing on the improvement of the quality of the already existing information e.g. by improving significantly the precision of measurements. This work is an example for the second method in order to deepen the understanding of properties of hadronic matter, precisely, the value of the total width of the  $\eta'$  meson ( $\Gamma_{\eta'}$ ).

Although the value of  $\Gamma_{\eta'}$  is known since 30 years [1], there are only two measurements so far [1, 2] with results which are admittedly in agreement within the limits of the achieved accuracy, but the reported  $\sim 30\text{--}50\%$  errors cause the average of these values not to be recommended by the Particle Data Group (PDG) [3]. Instead, the value resulting from a fit to 51 measurements of partial widths, integrated cross sections, and branching ratios is quoted by PDG [3]. However, both values (the measured average and the fit result) are not consistent and, additionally, the value recommended by PDG may cause some difficulties when interpreting experimental data due to the strong correlation between  $\Gamma_{\eta'}^{\text{PDG}}$  and  $\Gamma(\eta' \rightarrow \gamma\gamma)$ . This is the case e.g. in the investigations aiming for the determination of the gluonium contribution to the  $\eta'$  meson wave function [4].

Though there is no theoretical prediction about  $\Gamma_{\eta'}$ , there is strong interest in the precise determination of  $\Gamma_{\eta'}$  to translate branching ratios (BR) into partial widths, especially for the  $\eta'$  meson decay channels to  $\pi^+\pi^-\eta$ ,  $\rho\gamma$ , and  $\pi^0\pi^0\eta$  as inputs for the phenomenological description of Quantum Chromo-Dynamics in the non-perturbative regime [5].

It is also worth to note that an improvement of the experimental resolution by an order of magnitude in comparison to previous experiments [1, 2] could resolve fine structures in the  $\eta'$  signal, which cannot be excluded *a priori*.

The above-mentioned examples visualise that a precise determination of  $\Gamma_{\eta'}$  will provide important information for a better understanding of meson physics at low en-

ergies and, in particular, for structure and decay processes of the  $\eta'$  meson. Therefore, a more accurate than so far determination of  $\Gamma_{\eta'}$  constitutes the main motivation for this thesis. A more detailed motivation for such studies is presented in Chapter 2.

This work focuses on a measurement of  $\Gamma_{\eta'}$  performed in 2006 at the cooler synchrotron COSY with the COSY-11 detector setup, where the  $\eta'$  mesons were produced in collisions of protons from the circulating beam with protons from the cluster target stream [6]. The measurement was carried out at five beam momenta very close to the  $\eta'$  production threshold. The identification of the  $pp \rightarrow pp\eta'$  reaction is based on the reconstruction of the four-momentum vectors of the outgoing protons and on the calculation of the  $\eta'$  meson four-momentum vector from energy and momentum conservation. The total width of the  $\eta'$  meson is directly determined from the missing mass spectra. The mass resolution of the COSY-11 detector was improved to such limits that  $\Gamma_{\eta'}$  could have been obtained directly from the mass distribution established with a precision comparable to the width itself. Applied improvements are: (i) measurement very close to the kinematic threshold to decrease the uncertainties of the missing mass determination, since at threshold the value of  $\partial(mm)/\partial p$  approaches zero ( $mm \equiv$  missing mass,  $p \equiv$  momentum of the outgoing protons), (ii) higher voltage at the drift chambers to improve the spatial resolution for track reconstruction, (iii) reduced width of the cluster target stream to decrease the effective momentum spread of the beam due to the dispersion and to improve the momentum reconstruction, and finally (iv) measurements at five different beam momenta to reduce the systematic uncertainties.

The principle of the measurement together with the description of the experimental setup is given in Chapter 3. Information about the calibration of the detectors used for the registration of the protons and checks of the experimental conditions can be found in Chapter 4. Further, in Chapter 5 the identification of the  $pp \rightarrow pp\eta'$  reaction and the extraction of the background-free missing mass spectra is presented. The value of  $\Gamma_{\eta'}$  was obtained via a comparison of the experimental missing mass distributions to the Monte Carlo generated spectra including the value of  $\Gamma_{\eta'}$  as a free parameter, as it is presented in Chapter 6 together with estimations of the statistical and systematic uncertainties. Finally, the discussion of the achieved result and conclusions are presented in the last chapter.

## Chapter 2

# Motivation for the determination of the total width of the $\eta'$ meson

The total width of an unstable particle may be defined as a full width at half maximum (FWHM) of its mass distribution.

The first information about the observation of a meson with the mass  $958 \text{ MeV}/c^2$  came out in May 1964 [7, 8]<sup>1</sup> together with an upper limit for the total width  $\Gamma_{\eta'} < 12 \text{ MeV}$ . Afterwards several investigations about the properties of the  $\eta'$  meson were performed (see e.g. [9–11]). Soon it became clear, that physics connected with the  $\eta'$  meson has many interesting puzzles.

One of the still unsolved problems are the values and nature of decay constants. The predictions made on the quark flavour basis are done under the assumption, that the decay constants in that basis follow the pattern of particle state mixing [12, 13]. The quark-flavor mixing scheme can also be used for calculations of pseudoscalar transition form factors [14] and the degree of nonet symmetry and SU(3) breaking [15]. Such studies can be done via measurements or calculations of inter alia  $\Gamma(\eta' \rightarrow \gamma\gamma)$  and  $\Gamma(\eta' \rightarrow \rho\gamma)$ . However, the pseudoscalar mixing angle depends on the still unknown and vigorously investigated gluonium content of the  $\eta$  and  $\eta'$  wave functions [4, 16–24]. There are indications about large contributions of glue in both  $\eta$  and  $\eta'$  mesons [16, 17] although at the same time there are phenomenological analyses showing no evidence of a gluonium admixture in these mesons [21]. On the quark flavour basis the physical states  $\eta$  and  $\eta'$  are assumed to be a linear combination of the states  $|\eta_q\rangle \equiv 1/\sqrt{2}|u\bar{u} + d\bar{d}\rangle$ ,  $|\eta_s\rangle \equiv |s\bar{s}\rangle$ , and  $|G\rangle \equiv |\text{gluonium}\rangle$  [21]:

$$|\eta\rangle = X_\eta|\eta_q\rangle + Y_\eta|\eta_s\rangle + Z_\eta|G\rangle, \quad |\eta'\rangle = X_{\eta'}|\eta_q\rangle + Y_{\eta'}|\eta_s\rangle + Z_{\eta'}|G\rangle, \quad (2.1)$$

where  $X^2 + Y^2 + Z^2 = 1$ , and a possible gluonium component corresponds to  $Z^2 > 0$ . Experimental results indicate values which differ from zero:  $Z_{\eta'}^2 = 0.06^{+0.09}_{-0.06}$  [20],

---

<sup>1</sup> $X_0$  was an other name for the  $\eta'$  meson at that time.

$Z_{\eta'}^2 = 0.14 \pm 0.04$  [22],  $Z_{\eta'}^2 = 0.11 \pm 0.04$  [4]. Here the values of  $\Gamma(\eta' \rightarrow \gamma\gamma)$  and  $\Gamma(\eta' \rightarrow \rho\gamma)$  are important as constraints for  $X_{\eta'}^2$  and  $Y_{\eta'}^2$ . However, the value of  $\Gamma_{\eta'}$  recommended by the PDG ( $\Gamma_{\eta'}^{\text{PDG}}$ ) is strongly correlated with  $\Gamma(\eta' \rightarrow \gamma\gamma)$  as the most precise determined quantity contributing to the fit procedure [3], what causes problems when both  $\Gamma_{\eta'}^{\text{PDG}}$  and  $\Gamma(\eta' \rightarrow \gamma\gamma)$  are needed for the interpretation of the results [4]. A direct measurement of  $\Gamma_{\eta'}$  would allow to determine partial widths independently of  $\Gamma(\eta' \rightarrow \gamma\gamma)$ .

The precise determination of  $\Gamma_{\eta'}$  will also allow to establish more precisely partial widths, useful in many other interesting investigations. For example, the partial widths of  $\eta' \rightarrow \pi^+\pi^-\pi^0$  and  $\eta' \rightarrow \pi^+\pi^-\eta$  are interesting as a tool for investigations of the quark mass difference  $m_d - m_u$  [25–27], which induces isospin breaking in Quantum Chromo-Dynamics (QCD) [5, 25, 28]. The box anomaly of QCD, which breaks the symmetry under certain chiral transformations, together with the axial U(1) anomaly, preventing the particle from being a Goldstone boson in the limit of vanishing light quark masses, can be explored via anomalous decays of  $\eta'$  into  $\pi^+\pi^-l^+l^-$  (with  $l = e, \mu$ ) in a chiral unitary approach [29]. In all above considerations values of partial widths of  $\eta'$  decays are necessary as input values or as the cross checks for the assumptions.

From the experimental point of view the partial width can be determined either by an extraction of the corresponding branching ratio, or by a measurement of the ratio of the corresponding branching ratio and the branching ratio of another decay channel. In the first method the value of the total width has to be known, whereas in the second approach the partial width of the second decay channel is required, which refers again to the first method and the determination of the total width (or to the decay into two photons)<sup>2</sup>.

Determinations of the total width of the  $\eta'$  meson via production processes were performed in '79 [1] and '94 [2]<sup>3</sup>, however, the achieved accuracy on the  $\sim 30\%$  and  $\sim 50\%$  level, respectively, is not sufficient for studies discussed above. The average value of the two measurements is  $\Gamma_{\eta'}^{\text{average}} = (0.30 \pm 0.09) \text{ MeV}$  [3].

The indirect determination of  $\Gamma_{\eta'}$  ( $\Gamma_{\eta'}^{\text{PDG}} = (0.205 \pm 0.015) \text{ MeV}$ ) based on partial widths and branching ratios, recommended by PDG [3], provides a satisfactory result due to the high number of accurate measurements of branching ratios and of the probability of the  $\eta'$  meson formation in two photons collisions. It is based on the fit of partial widths, two combinations of particle widths obtained from integrated cross sections and on 16 branching ratios. Altogether PDG uses 51 measurements for the fit [3].

<sup>2</sup>Only  $\Gamma(X \rightarrow \gamma\gamma)$  can be derived separately due to the calculated dependence between the production cross section of  $X$  in two photons collisions and partial width [30, 31].

<sup>3</sup>In fact, there is a third measurement of  $\Gamma_{\eta'}$  from 2004 obtained as a by-product during  $J/\psi$  decay studies [32], however, it is not used by the Particle Data Group.



The partial width of the  $\eta'$  meson decay into two photons is crucial in such approach and can be derived from the following equation (for details see e.g. [33–35]):

$$N_{\eta'} = \Gamma_{\gamma\gamma} \tilde{\sigma}(\gamma^* \gamma^* \rightarrow \eta') \text{BR}(\eta' \rightarrow X) \mathcal{L}_{ee} \epsilon, \quad (2.2)$$

where  $N_{\eta'}$  corresponds to the number of the  $\eta'$  mesons observed in the reaction chain  $e^+e^- \rightarrow e^+e^-\gamma^*\gamma^* \rightarrow e^+e^-\eta' \rightarrow e^+e^-X$ ,  $\Gamma_{\gamma\gamma}$  denotes the partial width of the  $\eta'$  meson decay into two photons,  $\text{BR}(\eta' \rightarrow X)$  denotes the branching ratio for a measured decay channel,  $\mathcal{L}_{ee}$  is the integrated luminosity, and  $\epsilon$  is the overall efficiency for the registration of the  $e^+e^- \rightarrow e^+e^-\gamma^*\gamma^* \rightarrow e^+e^-\eta' \rightarrow e^+e^-X$  reaction. However, one needs to keep in mind, that the estimation of the cross section ( $\tilde{\sigma}(\gamma^*\gamma^* \rightarrow \eta')$ ) depends on the form factor, which must be derived from theory [14, 31, 36] or from other experiments [37, 38].

Branching ratios are measured and therefore any theoretical prediction of partial width can be transformed to the value of the  $\Gamma_{\eta'}$ . However, the theoretical predictions are spread over a relatively large range of values. Older values e.g. 0.30-0.33 MeV [23] and  $< 0.35$  MeV [39] are in line with the value of  $\Gamma_{\eta'}$  extracted from the direct measurements [1, 2], whereas more recent theoretical results like e.g. 0.20 MeV [29] and 0.21 MeV [28] are consistent with the value obtained by the PDG group [3].

As it was shown, issues concerning the  $\eta'$  meson cover a broad part of modern nuclear and particle physics, however, the value of the  $\eta'$  total width as a tool for translating precise measured branching ratios to partial widths is not well determined (average value from two measurements), or is correlated with branching ratios (PDG fit value) preventing it from an independent usage of this quantities for the interpretation of various experiments. Moreover, based on the average or the fit procedure there are two different values of the  $\eta'$  total width available [3].

There is another reason to perform a direct precise measurement of the  $\Gamma_{\eta'}$ . In spite of the fact that the  $\eta'$  meson seems to be a well confirmed particle, it still does not fully match into the quark model. All predictions and fits are done under the assumption that the  $\eta'$  meson is in fact a single state. However, the most precise signal of the  $\eta'$  was observed in measurements with a mass resolution of  $\text{FWHM} \approx 1 \text{ MeV}/c^2$  [1, 40–42]<sup>4</sup> and one cannot *a priori* exclude the possibility that some structure would be visible at higher precision. Especially, since there was some confusion about a multiple structure of the  $\eta'$  signal [45, 46] and there were already situations, where a better accuracy disclosed double "peaks" where only one signal was predicted and observed with a poor resolution like the signal of the  $\omega$  meson decay into two pions [47] or

<sup>4</sup>In previous studies of the  $\eta'$  meson performed by COSY-11, DISTO and SPES3 groups not dedicated for the total width determination the achieved mass resolutions were comparable with the experiment performed in Rutherford Laboratory [1] and amount to about 0.8 [41], 1.2 [40, 41], 1.5 [42], 5.0 [43] and 25.0 MeV/ $c^2$  [44].

$a_1(1260)$ - $a_2(1320)$  observed at CERN [47], it is always worth to look at something more precisely.

As was shown in this chapter the present discrepancy of the values of the total width of the  $\eta'$  meson should be, at least partially, solved by a direct measurement with a precision by an order of magnitude better than achieved so far. The work presented in this thesis was motivated by the endeavour to achieve such a precision.

## Chapter 3

# Principle of the measurement – simplicity is beautiful

A measurement of a particle's total width can be performed via one of the following methods:

1. Extraction from the slope of the excitation function [2].
2. Determination of the life time.
3. Measurement of branching ratios [3].
4. Direct measurements of mass distributions:
  - (a) invariant mass distribution from a decay process;
  - (b) missing mass distribution from a production process [1].

The determination of the total width from the slope of the excitation function is model dependent due to the need of the knowledge of the influence from the final state interactions between the ejectiles on the total cross section. In case of the  $\eta'$  meson a direct measurement of the life time (decay length) is impossible at the present technological level, because the investigated meson decays in the average after  $10^{-21}$  s [3]. Method 3 was used by the Particle Data Group and it mostly relies on the measurement of the  $\Gamma(\eta' \rightarrow \gamma\gamma)$  partial width. A direct determination of  $\Gamma_{\eta'}$  from a decay process requires high precision (at the level of  $\sim 1$  MeV), difficult to achieved at present. The last mentioned method, based on the missing mass technique, was already used in the first and so far most precise direct measurement of  $\Gamma_{\eta'}$  [1].

In this thesis  $\Gamma_{\eta'}$  is determined via the direct measurement of the  $\eta'$  meson mass distribution. For this purpose the  $\eta'$  meson was produced in the  $pp \rightarrow pp\eta'$  reaction, which was investigated by determining the four-momentum vectors of protons in the

initial and final states, and the mass of the  $\eta'$  meson was derived using the missing mass technique according to the following equation:

$$m_X^2 = |\mathbb{P}_X|^2 = |\mathbb{P}_{beam} + \mathbb{P}_{target} - \mathbb{P}_1 - \mathbb{P}_2|^2, \quad (3.1)$$

where  $m_X$  and  $\mathbb{P}_X$  denote mass and four-momentum vector of the unregistered particle, respectively and the  $\mathbb{P}_1, \mathbb{P}_2$  stand for the four-momenta of the outgoing protons<sup>1</sup>. The value of  $\Gamma_{\eta'}$  will be derived by the comparison of the experimental missing mass distribution with a set of Monte Carlo generated distributions for several assumed values of  $\Gamma_{\eta'}$ .

High precision can be achieved in the close-to-threshold region for the  $\eta'$  meson creation due to considerably reduced uncertainties of the missing mass determination since at threshold the value of  $\partial(mm)/\partial\mathbf{p}$  approaches zero ( $mm$  = missing mass,  $\mathbf{p}$  = momentum of the outgoing protons) [49]. Additionally the signal-to-background ratio is higher close to threshold [49].

Since the experimental resolution for the missing mass determination depends on the excess energy ( $Q$ ) the measurement was performed at several beam momenta in order to better control and reduce the systematic errors.

The experiment was conducted using the proton beam of the cooler synchrotron COSY and a hydrogen cluster target. The outgoing protons were measured by means of the COSY-11 detector. In order to decrease the spread of the beam momentum the COSY beam was cooled. Furthermore the missing mass resolution was improved by decreasing the horizontal target size and taking advantage of the fact that due to the dispersion only a small portion of the beam momentum distribution was interacting with the target protons. Additionally as it will be discussed in detail in Section 3.2 the decrease of the interaction region improved the resolution of the momentum reconstruction of the outgoing protons.

### 3.1 COoler SYnchrotron COSY

At the COoler SYnchrotron COSY [50] polarised or unpolarised proton or deuteron beams can be accelerated in the momentum range from 600 to about 3700 MeV/c. Each kind of beam can later be used in the internal or external experiments. A schematic view of the accelerator part of COSY is presented in Figure 3.1. The COSY-11 detector was set up<sup>2</sup> at a bending section of the synchrotron. The COSY synchrotron is

<sup>1</sup>The momentum of the proton from the target can be neglected during missing mass calculation, because it is six orders of magnitude smaller than beam momentum and two orders of magnitude smaller than momentum spread of the beam [48].

<sup>2</sup>The discussed measurement was done during the last COSY-11 beam time in September and October 2006. The detector was dismantled in April 2008.

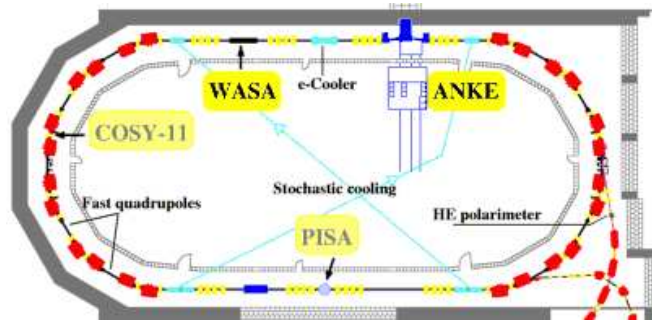


Figure 3.1: Schematic view of COSY. Dipoles and quadrupoles are plotted as red and yellow rectangles, respectively. Aqua colour denotes stochastic and electron cooling devices. Positions of present (WASA-at-COSY and ANKE) and completed experiments (COSY-11 and PISA) are shown. The figure is adapted from [51].

equipped with two kinds of beam cooling systems which allow for a reduction of the momentum and of the geometrical spread of the beam.

The principle of electron cooling is presented in Figure 3.2. The velocity of the electrons is made equal to the average velocity of the protons, but the velocity spread of electrons is much smaller compared to the protons. The electrons are inserted into the storage ring for a short distance where protons undergo Coulomb scattering in the electron *gas* and lose or gain energy, which is transferred from the protons to the co-streaming electrons, or vice versa, until some thermal equilibrium is attained [52, 53].

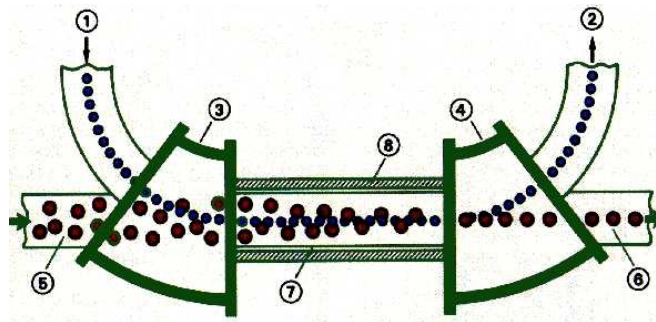


Figure 3.2: The principle of the electron cooling. Bigger purple dots represent protons, while smaller blue ones - electrons. 1. Insertion of electrons into the storage ring. 2. Extraction of the electrons. 3. and 4. Connection of the two ion pipes via toroids. 5. Uncooled proton beam. 6. Cooled proton beam. 7. Beam pipe. 8. Solenoid. The picture is adapted from [51].

Figure 3.3 presents the basic concept of stochastic cooling. It works in two steps. First, a measurement of the deviation from the nominal position of a part of the beam is performed, then this information is sent (by using a shorter way across the ring than the beam takes itself) to the opposite part of the ring where the position of the measured beam slice is corrected by electromagnetic deflection with a kicker unit [50]. Accidental mixing of the particles inside the beam causes that in each cycle different groups of the particles are corrected. The final effect occurs as a reduction of the momentum spread of the beam and as a decrease of the size of the beam [52–55]. COSY is equipped with vertical and longitudinal cooling elements which allow for the reduction of the emittance and decrease the momentum spread of the beam.

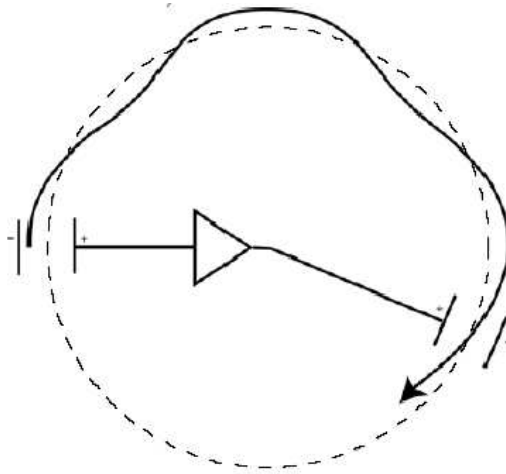


Figure 3.3: The concept of the stochastic cooling. The dashed line denotes the central beam orbit, while the solid arrow represents the trajectory of some beam particles. The figure is adapted from [56].

The above-mentioned properties of the COSY synchrotron ensure good quality of the beam (small momentum and geometrical spread) essential for precise measurements.

## 3.2 Cluster target

A cluster jet target [48] was used in all COSY–11 experiments. The schematic view of the target setup is presented in the left part of Figure 3.4. Purified hydrogen gas passes through a nozzle with an aperture diameter of  $\sim 16 \mu\text{m}$  and starts to condensate and forms nanoparticles called clusters. In order to separate the remaining gas from the clusters, the differential pumping stages with skimmers and collimators are used. The clusters have a divergence defined by the set of collimators and cross the COSY

beam defining the reaction region and finally enter the beam dump. The size of the reaction region influences the  $\Gamma_{\eta'}$  measurement in two ways. Firstly, the target setup is positioned in a bending section of the COSY ring in a dispersive region. It causes particles with different momenta to pass the target area at different horizontal positions. Therefore, the size of the target stream in a dispersion region defines the effective

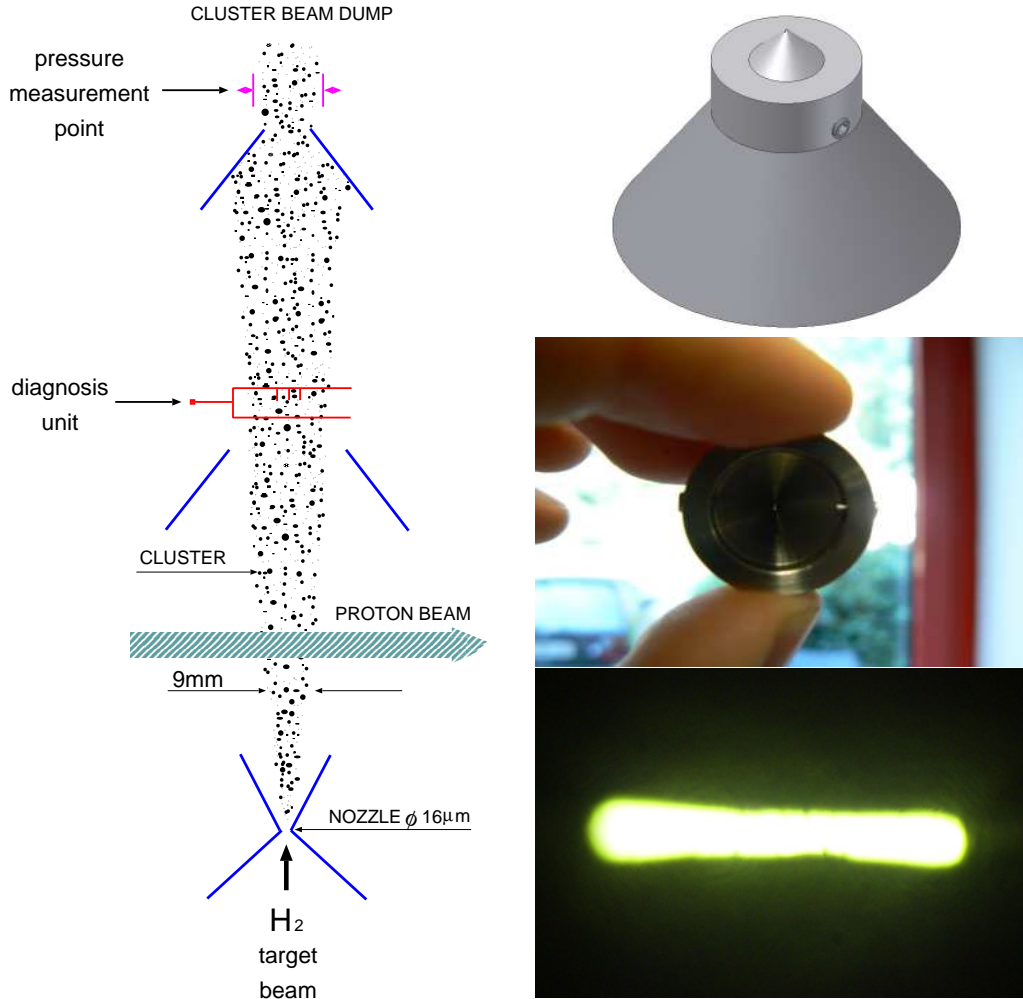


Figure 3.4: **Left:** Schematic view of the cluster target setup used in the COSY–11 detector setup. A collimator with a  $0.7 \times 0.07$  mm slit-shaped opening was used additionally to the  $\varnothing = 16 \mu\text{m}$  nozzle resulting in a target width of about 1 mm. A description of the usage of the wire device diagnosis unit is given in Section 4.3.1. The picture is adapted from [18]. **Right Top:** Collimator used during the  $\Gamma_{\eta'}$  measurement. The figure is adapted from [57]. **Right Middle:** Photo of the collimator from the upper part of the picture. The opening hardly is visible as a "white dot" in the centre of the collimator. **Right Bottom:** Photo of the slit in the new collimator taken with a transmitted light microscope. The photo is adapted from [57].



spread of the beam momentum, if only the geometrical size of the stream is smaller than the beam. Secondly, the point of the  $pp \rightarrow pp\eta'$  reaction is known only within the precision of the size of the reaction region which is defined as a cross section of the COSY beam and the target stream. Since the measurement of the momenta of the outgoing protons is based on the reconstruction of their trajectories (determined from the detectors) to the centre of the reaction region, the size of the reaction region has an influence on the accuracy of the momentum reconstruction. Those circumstances induced us to modify the collimator of the target setup. A slit shaped opening for the collimator was used instead of a circular opening, in order to provide a smaller effective spread of the beam and a better reconstruction of the momenta of the outgoing protons. The used collimator had a size of about 0.7 mm by 0.07 mm instead of a diameter of 0.7 mm [57]. This modification ensures a decrease of the horizontal size of the target stream in the reaction region down to  $\sim 1$  mm in the direction perpendicular to the beam line and  $\sim 9$  mm in the direction along the beam<sup>3</sup>. The size of the target stream along the COSY beam axis was not reduced since the resolution of the momentum reconstruction is not sensitive to the spread in this direction.

In order to determine the new size and position of the target stream a special diagnosis unit was designed and used. A detailed description of the method used for the determination of the target properties constitutes the subject of Section 4.3.1.

### 3.3 COSY–11 detector setup

The COSY–11 detector setup was designed as a magnetic spectrometer used for close-to-threshold studies of the production of light mesons. It was described in details in many previous publications e.g. [19, 58–62] therefore here it is only briefly presented. The principle of the operation of the COSY–11 system is visualised in Figure 3.5 which shows the most important detectors for the measurement of the  $pp \rightarrow pp\eta'$  reaction. At the left fraction of the picture one can see a part of the COSY ring: beam pipe, quadrupole and dipole magnets. The target setup (not shown in the figure) is mounted between the quadrupole and the dipole magnets. In case when a proton from the circulating beam hits a proton from the cluster target stream and a meson is created, both protons, as a consequence of a collision, have smaller momenta than the protons in the beam. Therefore, the reaction protons are bent stronger in the magnetic field of the dipole. Trajectories of the two outgoing protons are shown as green traces in Figure 3.5. The protons leave the dipole through a special foil made of carbon fiber layers fixed with epoxidy glue and coated with aluminium, which has a low mean nuclear charge to reduce straggling in the exit window [58]. Next, the protons fly through two

<sup>3</sup>In the previous experiments the target was crossing the beam as a stream with diameter of 9 mm.



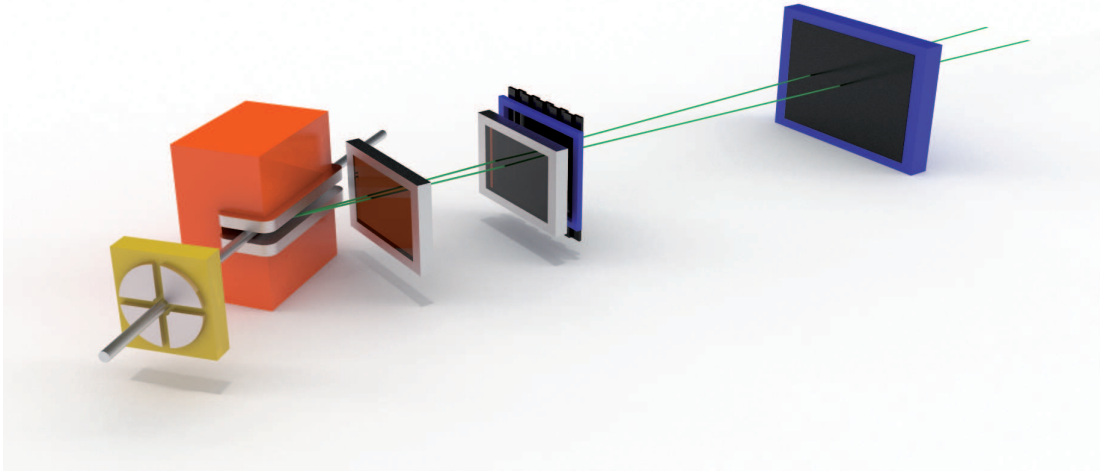


Figure 3.5: COSY-11 detector setup. From left to right: quadrupole (yellow) and dipole (orange) magnets of COSY, two drift chambers (silver) and two scintillator detectors (blue-black). (Picture courtesy of Barbara Wybieralska)

drift chamber stacks D1 and D2 and through scintillator detectors S1, S2 and S3 (see Figure 3.6). The measurement of the paths of the outgoing protons by means of the drift chambers allows for the reconstruction of the trajectories back through the known magnetic field to the assumed centre of the reaction region. As an output of this procedure one gets the momenta of the measured particles. Additionally, the velocity of particles is measured by the Time-of-Flight method (ToF) by means of the scintillator detectors S1 and S3. The information about the time when a particle crosses each detector together with the known trajectory allows to calculate its velocity. The independent determination of particle momentum and velocity enables its identification via its invariant mass. Since the momentum is reconstructed more precisely than the velocity, after the identification the energy of the particle is derived from its known mass and momentum. The measured four-momentum vectors of the outgoing protons and the well defined properties of the beam and target allow to calculate the mass of an unobserved particle based on the four-momentum conservation (Eq. 3.1).

Figure 3.6 shows a schematic top view of the COSY-11 detector setup. In addition to Figure 3.5 the vacuum chamber inside the dipole, the scintillator detectors S2 and S4, as well as the part of the silicon pad monitor detector Si are presented. S1 and S2 consist both of 16 separate vertically oriented scintillator modules with 10 cm width for S1 and 1.3 cm width in case of S2. The light from the scintillators is read out by photomultipliers at the lower and upper edge of each module. The higher granularity of S2 is helpful for triggering of events when two trajectories within one event are

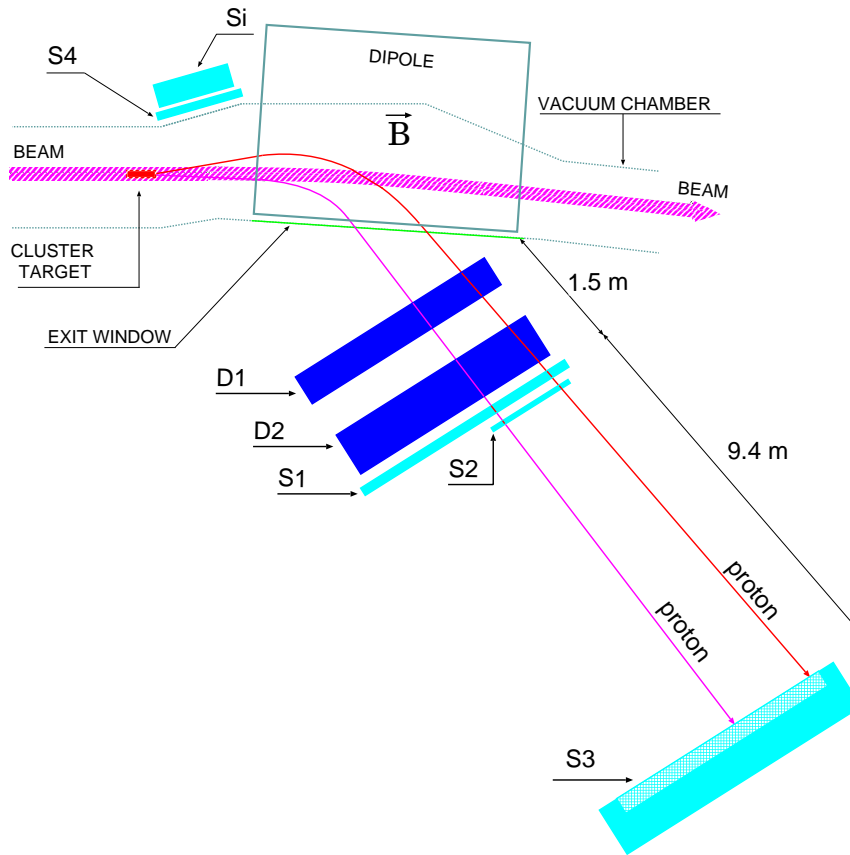


Figure 3.6: Schematic view of the COSY-11 detector setup (top view). Additionally, in comparison to picture 3.5, detectors S2, S4 and Si are shown. The picture is adapted from [18].

very close and cross the same module of S1. In this case they are separated with S2 as long as they are not crossing the same module of the S2. The positioning of the S2 detector was adjusted based on Monte Carlo simulations, prior to performing the experiment [49].

Detector S3 (scintillator wall) consists of one block of a  $220 \times 100 \times 5 \text{ cm}^3$  scintillator. A light signal generated by energy loss of a charged particle inside the scintillator is read out by a matrix of 217 photomultipliers. The centre of gravity of the signal amplitudes from individual photomultipliers is calculated in order to determine the hit position of a particle.

Detectors S4 and Si were used for the measurement of elastically scattered protons. One of the protons is tagged in the scintillator detector S4 and registered in the silicon pad detector Si consisting of 144 silicon pads with the dimensions  $22 \times 4.5 \times 0.28 \text{ mm}^3$ . The pads are arranged in three layers.

For the purpose of the experiment discussed in this dissertation, additionally, to the decrease of the horizontal target size, the accuracy of the momentum reconstruction

of the outgoing protons was also improved at the detector level. The high voltage of the drift chambers was increased (from 1600 to 1800 V) to achieve a better spatial resolution of the track reconstruction. This was never done before, since such a high precision was never necessary and the new settings of the high voltage were slightly above the standard structural safety operational level for the COSY-11 drift chambers. The applied change of high voltage caused an improvement of the spatial resolution of the drift chambers from  $\sim 250$  to  $\sim 100 \mu\text{m}$ .



# Chapter 4

## First steps on the way to the total width

The measurement for determining the total width of the  $\eta'$  meson conducted by the COSY-11 collaboration took place in September and October 2006. During 23 days of data taking<sup>1</sup> about 360 GB of raw data were collected from proton-proton collisions for five different beam energies. This chapter describes the selection of events corresponding to the  $pp \rightarrow pp\eta'$  reaction and the determination of the experimental conditions.

### 4.1 Preselection of data

Due to the high interaction rate and limited data transfer a selective hardware trigger was applied during the experiment. The triggering of the data acquisition was based on a selection of signals from scintillator detectors S1, S2, S3 and S4. The identification of the  $pp \rightarrow pp\eta'$  reaction requires the measurement of the two outgoing protons. Therefore the  $pp \rightarrow pp\eta'$  event candidate was stored if signals from two positively charged outgoing particles were present, which required fulfilment of one of the following conditions:

- signals from at least two modules of the S1 detector (multiplicity larger or equal to 2,  $S1_{\mu \geq 2}$ ).
- high amplitude signal from one module of the S1 detector ( $S1_{\mu=1, \text{high}}$ ), which corresponds to two (or more) particles passing through one module.
- signals from at least two modules of the S2 detector ( $S2_{\mu \geq 2}$ ).

---

<sup>1</sup>This period includes 4 days break due to a cyclotron failure.

In addition to these conditions coincident signals from at least three photomultipliers (PM) in the S3 detector were required ( $S3_{\mu_{PM} \geq 3}$ ) [18]. The complete trigger condition for a  $pp \rightarrow pp\eta'$  event candidate can be written as:

$$\{S1_{\mu \geq 2}^{2...5} \vee S1_{\mu=1, \text{high}}^{3...5} \vee S2_{\mu \geq 2}^{1...16}\} \wedge S3_{\mu_{PM} \geq 3}, \quad (4.1)$$

where superscripts denote the range of modules taken into account for the calculations of the multiplicity  $\mu$ . This range was established according to simulation of the  $pp \rightarrow pp\eta'$  reaction [49]. Based on the data, the threshold for the  $S1_{\mu=1, \text{high}}^{3...5}$  signals was adjusted such that a significant amount of one track events was discriminated with the negligible loss of two protons events [63].

In addition, elastically scattered  $pp \rightarrow pp$  event candidates were stored for monitoring target and beam properties described in detail in Section 4.3.2. The trigger conditions in this case required a signal in exactly one module in the S1 hodoscope in coincidence with one signal in the S4 detector (see Figure 3.6).

As the first step in the *off-line* analysis the stored events were grouped into two categories:  $pp \rightarrow pp$  and  $pp \rightarrow pp\eta'$  event candidates. This selection was based on the signals from the drift chambers. The first group was used for the adjustment of the position of the drift chambers, determination of the relative beam momenta, and monitoring of the target stream properties, while the second group was used for the calibration of the detectors and the determination of the total width of the  $\eta'$  meson. The purpose of this procedure is to reduce the amount of data significantly without the application of a CPU time consuming reconstruction. To receive event samples as clean as possible without using reconstruction procedures as a selection criterion the number of drift chamber wires with a signal above a certain threshold was used. The drift chambers D1 and D2 consist in total of 14 planes (6 and 8, respectively). Therefore in an ideal case 14 signals are expected for the  $pp \rightarrow pp$  reaction and 28 for  $pp \rightarrow pp\eta'$  because in the first case only one proton passes through the chambers and in the second case two protons must be registered (see Figure 3.6). Based on the experience gained in previous COSY-11 experiments [18, 19, 40, 59, 64] the conditions for optimising the efficiency and the time of the reconstruction were obtained when requiring that at least 12 planes responded with signals to one passing particle. Therefore for the  $pp \rightarrow pp$  event candidate additionally to signals in the S1 and the S4 detectors at least 12 signals in drift chambers were required. Whereas for the  $pp \rightarrow pp\eta'$  candidates signals in the S1 (or S2) and the S3 detectors and at least 24 signals in drift chambers were demanded<sup>2</sup>.

---

<sup>2</sup>For the purpose of the described selection the number of *signals* in the drift chamber in the case of the  $pp \rightarrow pp$  reaction is defined as the number of planes with at least one "fired" wire, whereas in the case of the  $pp \rightarrow pp\eta'$  reaction the number of *signals* means the number of "fired" wires, with the restriction that 2 or more "fired" wires in one plane are counted as exactly 2.

Using the above conditions the full sample of  $2.1 \times 10^8$  registered events was reduced to  $1.1 \times 10^8$   $pp \rightarrow pp$  candidates and to  $1.6 \times 10^7$   $pp \rightarrow pp\eta'$  candidates.

## 4.2 Calibration of detectors

There were only two kinds of detectors used for the identification of the  $pp \rightarrow pp\eta'$  reaction: the drift chambers (D1, D2) and the scintillator detectors (S1, S2 and S3). In the following section their calibration based on the collected data is presented.

### 4.2.1 Drift chambers

The calibration of the drift chambers proceeded in three steps. First the relative time offsets between all wires were adjusted, next the relation between the drift time and the distance to the wire was established and finally relative geometrical settings of the drift chambers were optimised.

#### 4.2.1.1 Relative time offsets of wires

The measured drift time of the electrons  $t_{drift}$  can be calculated from a difference between the time signals from the drift chambers and from the S1 detector. The arrival times of the signals from those detectors at the Time to Digital Converters (TDC) are described by following equations:

$$TDC_{DC} = t_{stop}^{DC} - t_{start}^{trigger} \quad TDC_{S1} = t_{stop}^{S1} - t_{start}^{trigger}, \quad (4.2)$$

where  $t_{start}^{trigger}$  denotes a common start signal for an event and  $t_{stop}^i$  denotes the stop signal from  $i$ -th detector, which is a sum of the following terms:

$$t_{stop}^{DC} = t_{DC}^{real} + t_{drift} + C_{DC}^k \quad t_{stop}^{S1} = t_{DC}^{real} + \Delta t_{DC-S1} + C_{S1}, \quad (4.3)$$

where  $t_{DC}^{real}$  defines the real time when the particle passes through the drift chamber,  $\Delta t_{DC-S1}$  gives the time of flight of the particle between DC and S1,  $C_{S1}$  is a constant corresponding to the time offset of the S1 detector and  $C_{DC}^k$  stands for the time offset of the  $k$ -th wire of the drift chamber. The difference between the time signals from the drift chamber and the S1 scintillator can then be written as:

$$TDC_{DC} - TDC_{S1} = t_{stop}^{DC} - t_{start}^{trigger} - t_{stop}^{S1} + t_{start}^{trigger} = t_{drift} + \underbrace{C_{DC}^k - \Delta t_{DC-S1} - C_{S1}}_{C^k}. \quad (4.4)$$

The  $C^k$  offsets were adjusted based on the leading edge of the drift time spectra (see Figure 4.1). The  $\Delta t_{DC-S1}$  depends on the particle velocity. However, for protons from

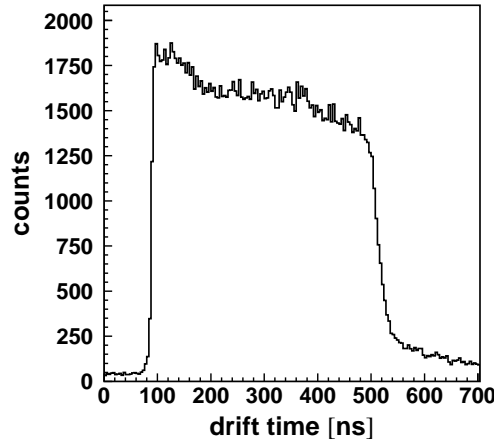


Figure 4.1: Typical spectrum of the drift time for a single plane.

the  $pp \rightarrow pp\eta'$  reaction (even at the largest access energy ( $Q = 5$  MeV) studied) it varies only from 0.72 to 0.78 (in speed of light units) and results in a variation of  $\Delta t_{DC-S1}$  in the order of  $\sim 0.3$  ns, which can be neglected in view of the 400 ns drift time for 20 mm distance (size of the one cell). The offsets were set for each plane separately. This allows to make a single space-time calibration for all cells in one plane.

#### 4.2.1.2 Time-space calibration

The time-space calibration of the drift chamber is a procedure to obtain the dependence between drift time and the distance of the track to the sense wire. Charged particles crossing the drift chamber cause gas ionisation and generate electron clusters moving towards the anode wires. The drift time of those electron clusters ( $t$ ) can be transformed to the minimum distance between the trajectory of a particle crossing the drift chamber and the sense wire ( $d$ ). The relation between drift time and the minimum distance ( $d(t)$ ) has to be derived from the experimental data and, to minimise the influence of variations like atmospheric pressure, air humidity and gas mixture changes [65] on the drift velocities, it should be determined separately for different periods of data taking. In this analysis  $\sim 22$ -24 hours periods were used.

The calibration method is based on the assumption that the trajectory of a particle crossing the drift chamber is a straight line. Starting with the approximate time-space function  $d(t)$ <sup>3</sup> the minimum distance between trajectory and the sense wires were calculated. Then, a straight line was fitted to the obtained set of points. The minimum

<sup>3</sup>As the approximate calibration a function determined in the previous experiment was used. In general one can extract the space-time relation from the shape of the drift time distribution using the "uniform irradiation" method [66, 67].



distance between the fitted line and the sense wire for  $i$ -th event is denoted as  $d_i^{fit}(t)$ . The correction  $\Delta d(t)$  of the approximate time-space function  $d(t)$  has been calculated as a function of the drift time  $t$  from the following equation:

$$\Delta d(t) = \frac{1}{n} \sum_{i=1}^n (d_i(t) - d_i^{fit}(t)) , \quad (4.5)$$

where  $n$  denotes the number of entries in the data sample. Then the new calibration function was calculated as:

$$d^{new}(t) = d(t) - \Delta d(t) . \quad (4.6)$$

The above procedure was repeated until  $\Delta d(t)$  became negligible in comparison to the spatial resolution of the chamber. An example of the calculated time-space function for an arbitrarily chosen sense wire in DC1 is presented in Figure 4.2 (left). In the right plot, for an arbitrarily chosen plane of DC1, the middle line corresponds to the average difference  $\Delta d(t)$  while the upper and lower lines denote one standard deviation of the  $(d_i(t) - d_i^{fit}(t))$  distribution. As can be inferred from the right plot of Figure 4.2 the achieved spatial resolution amounts to about  $100 \mu\text{m}$  over the whole drift time range except for the small area very close to the sense wire.

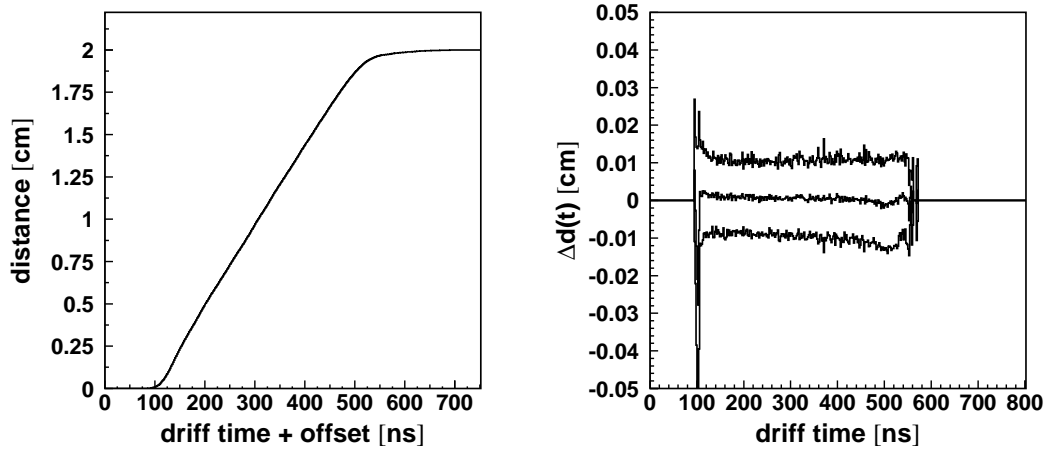


Figure 4.2: **Left:** Distance from the particle trajectory to the sense wire as a function of the drift time. **Right:** Average deviation  $\Delta d(t)$  between the measured and the fitted distances of tracks from the sense wire as a function of the drift time as obtained after the second iteration (see text). The distribution around  $\Delta d = 0$  corresponds to the correction  $\Delta d(t)$  and the lines around  $\pm 0.01$  cm denote one standard deviation of the  $(d_i(t) - d_i^{fit}(t))$  distribution.

#### 4.2.1.3 Relative positions of the drift chambers

The relative geometrical setting of the drift chambers was established based on the quality of the fit of a straight line to the distances of the particle trajectory to the sense wires in both drift chambers. The idea of the method is schematically presented in Figure 4.3. Based on the  $\chi^2$  distribution of the fit the relative position of the chambers was found to be  $\Delta x = 1.4$  mm,  $\Delta y = -1.8$  mm and  $\Delta z = 0.5$  mm (the statistical errors are negligible). Typical spectra of the  $\chi^2$  values for X and Y directions are presented in Figure 4.4. The larger absolute changes of  $\chi^2$  for variations of the  $\Delta X$  than for the  $\Delta Y$

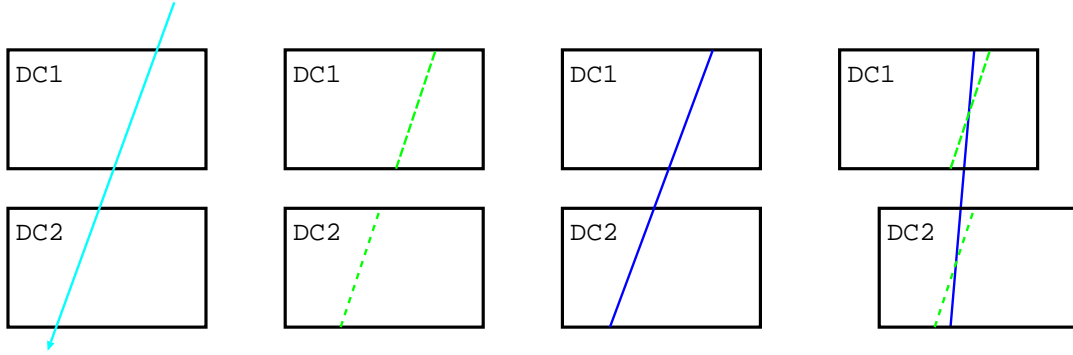


Figure 4.3: The idea of the derivation of the relative position of the drift chambers. From left to right: (top view of the drift chambers pairs) a charged particle crosses two drift chambers (trajectory plotted as cyan arrow); positions of the trajectory (green) in each plane (derivation based on the calibration); straight line (blue) fitted to position information from the drift chambers, in case when the relative position of the drift chambers is known correctly; the same as before but in case when there is a discrepancy between nominal and real position of the detectors.

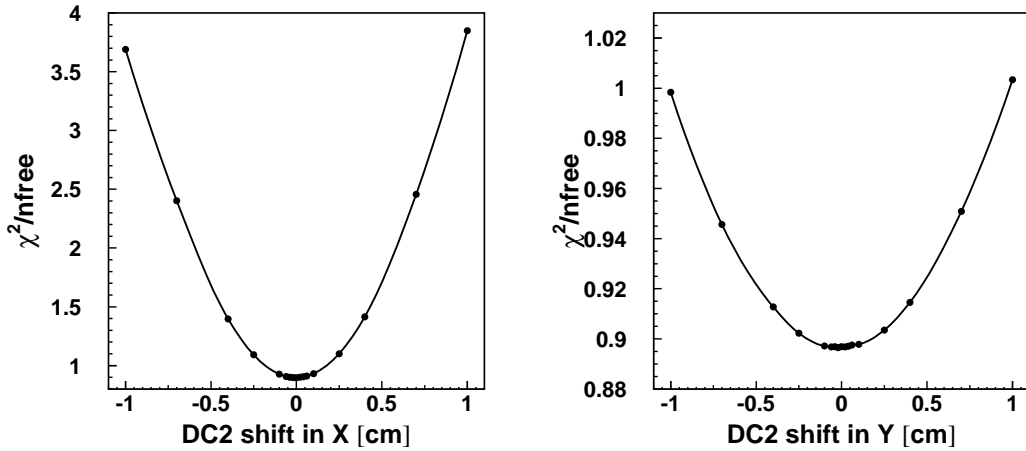


Figure 4.4: Value of reduced  $\chi^2$  for the fit of the straight line to the signals from both drift chambers as a function of their relative position in X (left) and Y (right) direction.

direction correspond to the better spatial resolution of the drift chambers in X direction compared to the Y direction. This is due to the construction of the planes with wires oriented both vertically and inclined by  $\pm 31^\circ$  [58].

After the relative adjustment of the drift chambers, their position with respect to the dipole was established based on  $pp \rightarrow pp$  events. Details are presented in Section 4.3.2.

### 4.2.2 Timing of scintillator detectors

The detectors S1 and S3 used for particle identification in the time-of-flight method were calibrated in order to adjust time offsets for particular photomultipliers (PM). S1 consist of 16 scintillating modules read out by photomultipliers on both sides, while S3 is a scintillator wall read out by a matrix of 217 photomultipliers. The time-of-flight is defined as the difference between times of crossing the S1 and S3 detectors ( $ToF = t_{S3} - t_{S1}$ ). For the calibration of the scintillator counters we compare the time-of-flight obtained from signals registered in the S1 and S3 detectors and the time-of-flight calculated from the reconstructed momentum of the particle.

The experimentally available TDC values depend on the time when a particle crosses the detectors ( $t_{S1}, t_{S2}$ ) plus the propagation time of the created light and electrical signals. In general, it may be expressed as:

$$\begin{aligned} TDC_{S1}(PM) &= t_{S1} + t(y) + t_{S1}^{walk}(PM) + t_{S1}^{offset}(PM) - t_{trigger} \\ TDC_{S3}(PM) &= t_{S3} + t(l) + t_{S3}^{walk}(PM) + t_{S3}^{offset}(PM) - t_{trigger}, \end{aligned} \quad (4.7)$$

where  $t_{trigger}$  denotes the time of the trigger signal,  $t(y)$  denotes the time of light propagation for the distance between the cross point in the S1 module and the scintillator edge and  $t(l)$  stands for the time of light propagation for the distance between the hit position in S3 and the photomultiplier. Due to the usage of leading edge discriminators a *time walk effect* is present, i.e. a variation of the registered TDC time  $t^{walk}(PM)$  as a function of the signal amplitude. The correction of this effect can be done by applying the formula  $t^{walk}(PM) \approx constant \times (ADC)^{-\frac{1}{2}}$ , where  $ADC$  denotes the signal charge value [68]. Since the  $t_{trigger}$  values are the same in both equations 4.7 for computation of  $ToF$  only time offset values  $t^{offset}(PM)$  are unknown. However, they can be obtained by a comparison of the  $ToF$  value based on the signals from scintillators  $ToF_{S1-S3}$  and the time-of-flight value calculated from the reconstructed particle momentum  $ToF_{mom} = l/\beta$ , where  $l$  is the path length between the S1 and the S3 detectors obtained from the trajectory reconstructed in the drift chambers, and  $\beta$  is the particle velocity calculated from the reconstructed momentum with the known mass, with the identification of the particle based on the invariant mass distribution resulting with time offsets determined in former experiments. Having approximate values of

$t_{S1}^{offset}(PM)$  the time offsets for the photomultipliers in the S3 detector can be determined. Then, using the determined values of  $t_{S3}^{offset}(PM)$  the new set of  $t_{S1}^{offset}(PM)$  can be calculated. After a few iterations the offsets for both detectors were obtained.<sup>4</sup>

As an example the plots in Figure 4.5 present results of the calibration for arbitrarily chosen photomultipliers (PM) of the S1 and S3 detectors.

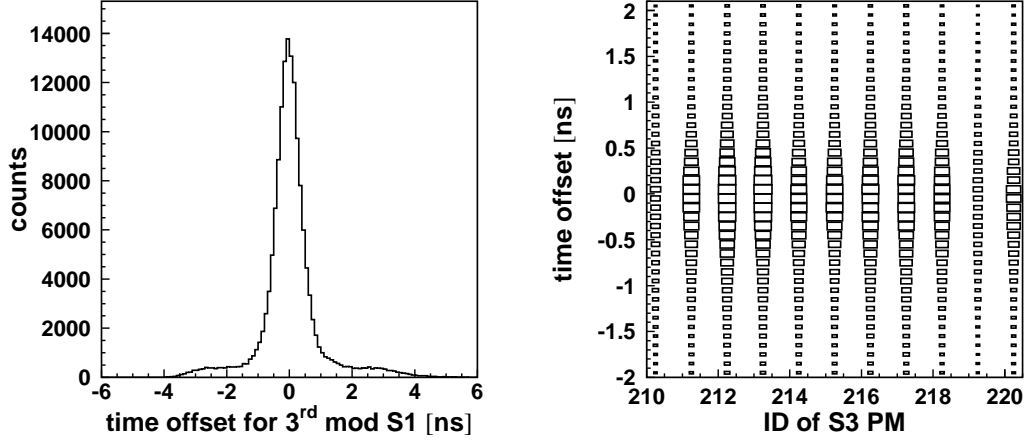


Figure 4.5: Distributions of the difference determined from the time-of-flight measured between the S1 and the S3 detectors and the time-of-flight calculated from the momentum reconstructed based on the curvature of the trajectory in the magnetic field. As an example spectra for the 3<sup>rd</sup> S1 module and an exemplary range of photomultipliers (PM) of the S3 detector are shown. The counting rate of PM 210 and 219 is smaller since these photomultipliers are positioned at the edges of the detector.

### 4.3 Properties of the cluster target stream

Since the momentum determination of the outgoing particles is based on the track reconstruction to the centre of the reaction region (for details see Section 5.1), the size and position of the target stream influence the experimental momentum reconstruction significantly, and the accuracy of their determination will reflect itself in the determination of systematic uncertainty of the resolution of the missing mass spectra. Therefore, the properties of the cluster target were monitored via two independent methods: using a dedicated diagnosis unit and inspecting a kinematic of  $pp \rightarrow pp$  events.

<sup>4</sup>In case of the S1 detector, further on in the analysis of the  $pp \rightarrow pp\eta'$  reaction the average of times from upper and lower photomultipliers were used.

### 4.3.1 Diagnosis unit – wire device

The diagnosis unit was developed for the measurement of the position and size of the target stream. Figure 4.6 presents a photo of the tool. As shown schematically in the left part of Figure 3.4 it was installed above the reaction region downstream the target beam<sup>5</sup>, allowing for the monitoring of the size and position of the target concurrently to the measurements of the  $pp \rightarrow pp\eta'$  reaction.



Figure 4.6: Photography of the diagnosis unit. For the description see text.

The monitoring of the target properties above the beam line permits to interpolate the target position and size to the reaction region taking into account the distance between collimator and reaction region ( $\sim 59$  cm), and the distance between reaction region and diagnosis unit ( $\sim 71$  cm).

The diagnosis unit (shown in Figure 4.6) consists of three *arms*: two wires with diameters of 1 mm and 0.1 mm (hardly visible in the photo) and a broad *arm*, the part with holes and three short perpendicular wires<sup>6</sup>.

During the measurement the diagnosis unit rotates with constant angular velocity around the axis perpendicular to the target stream. The *arms* cross the target stream one by one, which cause changes of the pressure in the stage above the diagnosis unit (see the left part of Figure 3.4). The measured pressure values are presented in the upper left part of the Figure 4.7 as a function of time. The sixfold structure visible in the plot corresponds to the different *arms* of the diagnosis unit crossing the target stream (each *arm* crosses the stream twice during a full rotation, once at the top and

<sup>5</sup>As shown in the left part of Figure 3.4 the target stream moves from the bottom to the top.

<sup>6</sup>The usage of three perpendicular wires allowed for the determination of the target inclination.

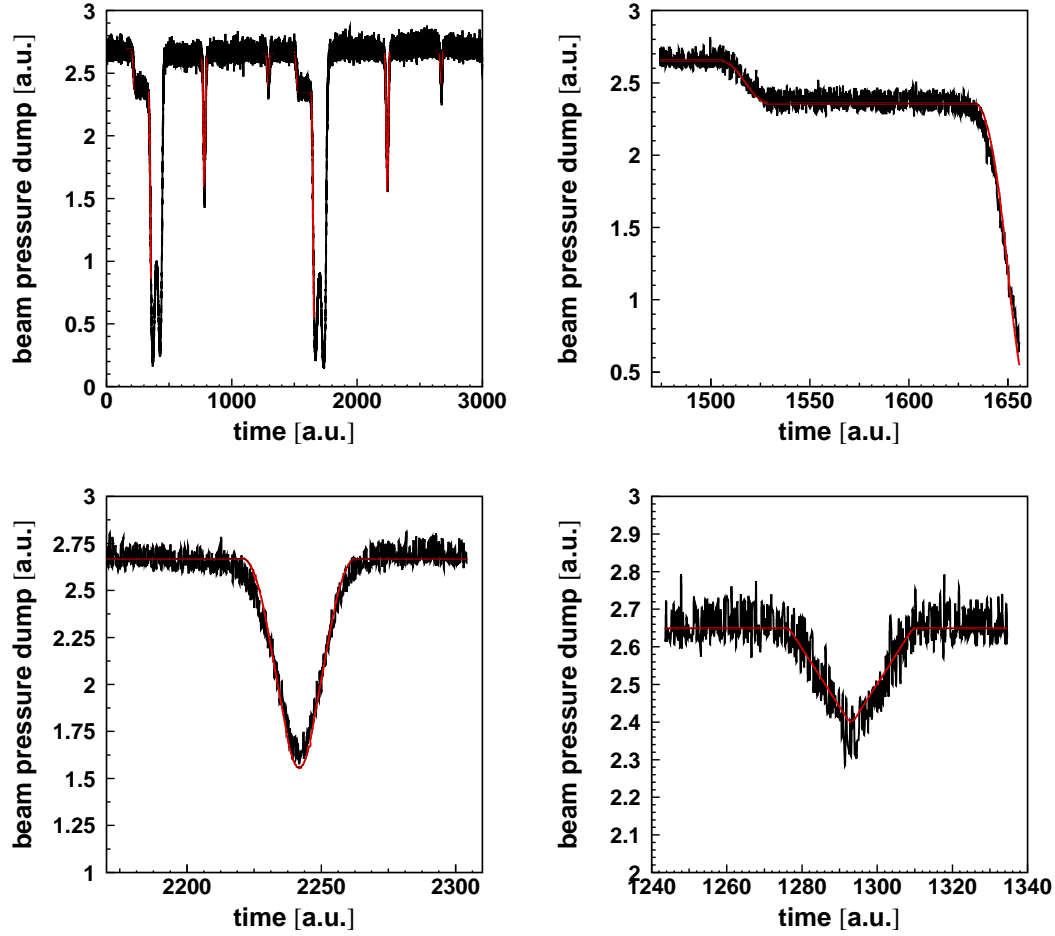


Figure 4.7: Example of changes of the target stream pressure as a function of the rotation time of the diagnosis unit (black). Red lines correspond to the result of the simulation. **Upper left:** Full cycle of the rotation. **Upper right:** Close-up of the minimum due to the *broad* arm and three short wires. **Lower:** Close-ups of the minima due to the thick (**lower left**) and thin (**lower right**) wire passage. The width of the *plateau* at the top of the pictures corresponds to the pressure fluctuations.

a second time at the bottom). The rotation was realised by a step motor and the full rotation cycle took 2400 steps. The first structure in the upper left part of the Figure 4.7 corresponds to the passage of the *broad arm* with three perpendicular wires (the small *step* at the leading edge) and the part with holes (the double-well structure). The next two sharp minima correspond to the crossing of the thick and thin wire, respectively. The amplitudes of the minima differ slightly depending whether the *arm* crosses the stream closer to or further from the pressure measurement region. The remaining plots in Figure 4.7 contain close-ups of structures from the upper left part.

The decrease of the measured pressure is proportional to the area of the wire blocking at a given moment the stream of the target. Therefore, knowing the size of the particular parts of the diagnosis unit and velocity of the rotation one can simulate the relative changes of the pressure as a function of time, under the assumption of the pa-

rameters describing the size, inclination (angle) and position of the target stream. The comparison of the results of simulations with the measured variations of the pressure allows to establish the parameters of the target based on the minimialisation of the  $\chi^2$ . The red lines in the plots in Figure 4.7 denote result of the simulation corresponding to the parameters for which the  $\chi^2$  is at a minimum value. The determined properties of the target stream in the reaction region are:

$$\begin{aligned}
 width &= (0.089 \pm 0.005) \text{ cm} \\
 length &= (1.053 \pm 0.005) \text{ cm} \\
 X - position &= (0.27 \pm 0.05) \text{ cm} \\
 Z - position &= (0.02 \pm 0.05) \text{ cm} \\
 angle &= (4.03 \pm 0.01) \text{ deg},
 \end{aligned} \tag{4.8}$$

where the position is calculated in the nominal target system reference frame and the angle is defined with respect to the beam direction. The quoted uncertainties of X and Z positions include the inaccuracy of the determination of the position of the diagnosis unit in the reference frame of the target. Size and relative position of beam and target stream are shown in Figure 4.8.

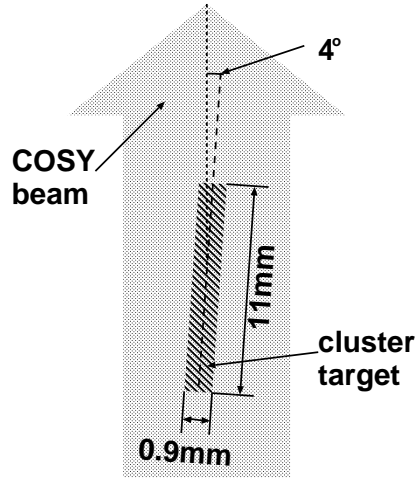


Figure 4.8: Size and relative position of beam and target stream determined from the measurement based on the diagnosis unit. (In this thesis a Z coordinate is defined along the COSY beam line.)

There were no changes of the target stream size, angle and X-position during the entire experimental period. However, there were changes of the Z position in the order of 1 mm. A quantitative discussion of this variations is presented in Section 4.3.3.

It is worth to stress that the target stream width, length and angle correspond to an effective target width of 1.06 mm.



### 4.3.2 Kinematic ellipse from $pp \rightarrow pp$ events

The second and independent method used for the determination of the target stream properties is based on the measurement of the momentum distribution of elastically scattered  $pp \rightarrow pp$  events.

Elastically scattered protons form an ellipsoid in momentum space in the LAB system. The projection of the momentum components ( $p_{\perp}$  = perpendicular,  $p_{\parallel}$  = parallel to the beam direction) constitutes an ellipse. The acceptance of the COSY-11 detector allows for the measurement of the lower right part of it (see left part of Figure 4.9).

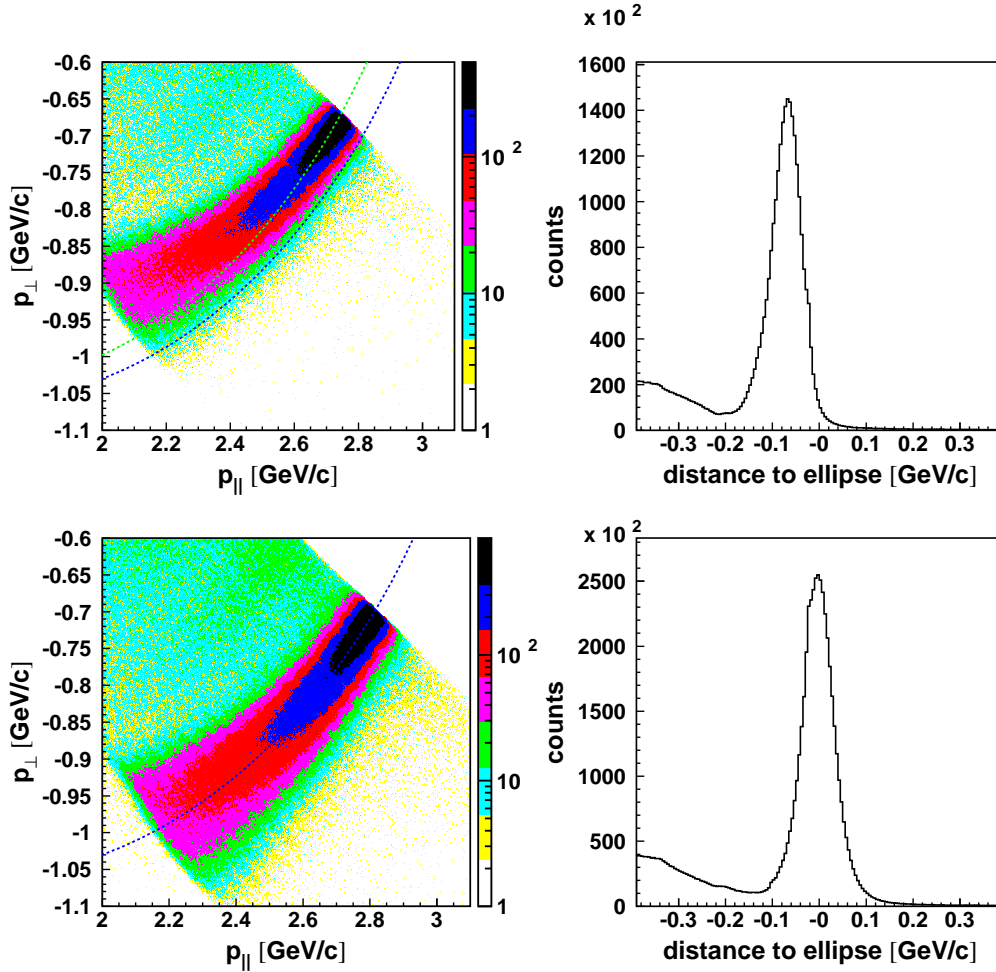


Figure 4.9: **Upper left:** Part of the experimental kinematic ellipse from  $pp \rightarrow pp$  events analysed for the nominal target stream position ( $x = 0$ ,  $z = 0$ ). The smooth change of the amplitude of the density distribution reflects the strong angular dependence of the  $pp \rightarrow pp$  cross section. Theoretical ellipses for beam momentum values 3211 MeV/c (nominal one) and 3111 MeV/c are plotted as blue and green lines, respectively. **Upper right:** Projection of the distribution from upper left plot along the theoretical blue ellipse. **Lower left:** The same data as for upper left plot but analysed for a target stream position of  $x = 2.35$  mm,  $z = 0$ . **Lower right:** Projection of the distribution from lower left plot along the theoretical blue ellipse.



The momentum reconstruction of positively charged particles in the COSY-11 detector is based on the determination of their trajectories by means of the drift chambers and the back-reconstruction through the known magnetic field to the reaction region (see Figure 3.6). Since the exact reaction point is known only with an accuracy determined by the size of the reaction region, defined as the overlap of the beam and the target stream, back-reconstruction is performed to the centre of this region. This causes the spread of the points around the calculated kinematic ellipse. Naturally the spread depends on the size of the reaction region, whereas the average shift of the points from the expected ellipse reflect a wrong assumption of the position of the centre of the reaction region. In principle the average shift may also be due to a wrong assumption of the absolute value of the beam momentum. However, as proven already in the previous analysis [69] it may be safely neglected taking into account the accuracy of the absolute beam momentum determination of 3 MeV/c [70]. For the illustration of the effect, the nominal beam momentum was decreased by 100 MeV/c (see Figure 4.9). One can estimate that an inaccuracy of 3 MeV/c would cause a negligible effect. The blue line denotes the expected ellipse for the nominal beam momentum of 3211 MeV/c, the green line for 3111 MeV/c. The projection of the experimental points along the expected ellipse (blue line) is presented in the upper right plot in Figure 4.9.

Moreover, the momentum reconstruction is very sensitive to the assumption of the centre of the interaction region. The ellipse presented in the upper left plot in Figure 4.9 was derived under the assumption that the target stream is at the nominal position ( $x = 0$ ,  $z = 0$ , the  $y$ -position is well defined by the plane of the circulating beam).

The ellipse in the lower left plot in Figure 4.9 was derived from the same data as for the ellipse from upper plot, however, the analysis was performed under the assumption of the target centre position:  $x = 2.35$  mm,  $z = 0$ . The blue theoretical ellipse follows the shape of the data, much better than for the (wrong)  $x = 0$  position, which is also visible in the projection in the lower right plot in Figure 4.9.

The value of the reconstructed momentum depends also on the assumed relative settings of the drift chambers, dipole magnet and the target. Therefore the momentum distributions of the  $pp \rightarrow pp$  events are also sensitive to the drift chamber position relative to the dipole. However, wrong assumption about the position of the drift chambers or about the position of the target modify those distributions in a different ways and therefore these positions can be established independently of each other.

To reduce the background contribution from the multibody production reactions two cuts were applied. First the squared missing mass to the  $pp \rightarrow pX$  reaction was calculated and then the range of the squared missing mass from 0.4 to 1.2 GeV<sup>2</sup>/c<sup>4</sup> was chosen for proton selection (see left plot in Figure 4.10). In addition, the two-body kinematics of elastic proton-proton scattering allows to combine the scattering angles  $\Theta_1$  and  $\Theta_2$  of the recoiled and forward flying protons. In the COSY-11 apparatus

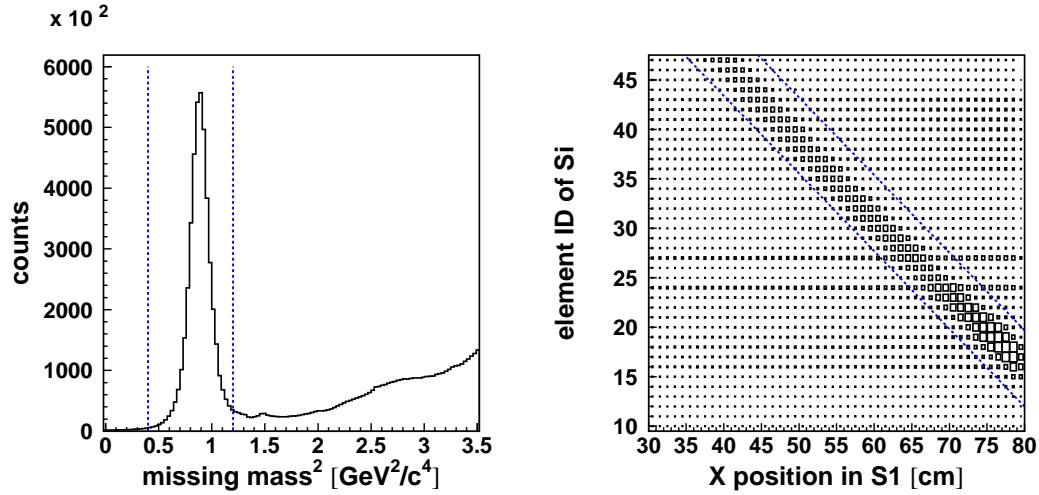


Figure 4.10: **Left:** Square of the missing mass to the  $pp \rightarrow pX$  reaction. A clear signal from the protons is visible. The blue dashed lines correspond to the applied cut. **Right:** Correlation between position of the registered particle in the S1 detector and the element number of the Si detector (see Figure 4.11). The blue dashed lines correspond to the cut range. The relative intensity increases in channels 24 and 27 of the Si detector are due to higher noise levels in these detector elements.

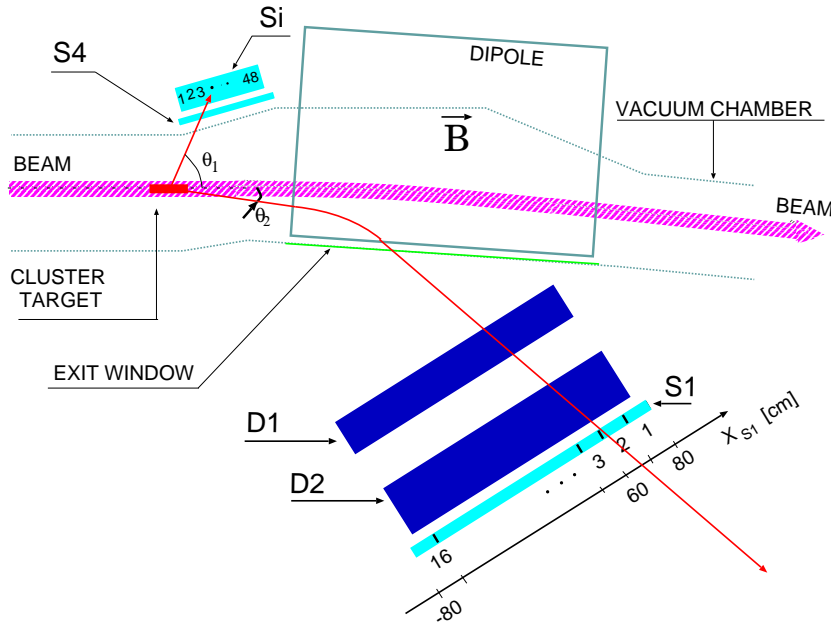


Figure 4.11: Close-up of the part of the COSY-11 detector used for the registration of elastically scattered events. The picture is adapted from [18].

the scattering angles correspond to the pad number of the silicon monitor detector (Si) and the position in the S1 detector (see Figure 4.11). The correlation is visible in the right plot in Figure 4.10. The cut was applied as indicated by the blue dotted lines. The applied cuts are tight, however, the absolute number of  $pp \rightarrow pp$  events is not substantial for the  $\Gamma_{\eta'}$  analysis. The kinematic ellipse and its projection along the theoretical curve with adjusted position of the target after applying the mentioned cuts is presented in Figure 4.12. A negligible amount of background remained.

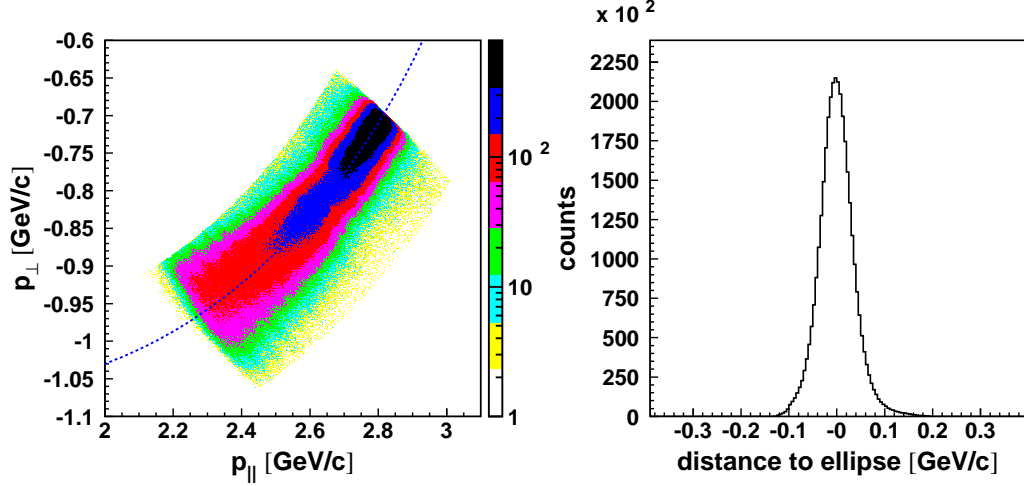


Figure 4.12: **Left:** Experimental kinematic ellipse from  $pp \rightarrow pp$  events analysed for the corrected position of the target and drift chambers after application of the cuts on the squared invariant mass and angles correlation spectra. The theoretical ellipse for the nominal value of the beam momentum is plotted as a blue line. **Right:** Projection of the distribution from left plot along the theoretical ellipse.

The simultaneous comparison of the theoretical ellipses with the experimental ones derived for five different beam momenta allows for the determination of position and effective width of the target and position of the drift chambers. The effective target width has an influence on the spread of points around the kinematic ellipse. However, in practise, based on the elastically scattered events one can determine the target width only if it is greater than  $\sim 0.2$  cm (as it is shown in Figure 4.13). Below 0.2 cm other effects dominate the contribution to the spread of the experimental points. The obtained results using the described method are:

$$\begin{aligned}
 \text{effective target width} &< 0.2 \text{ cm}, \\
 \text{target } X - \text{position} &= (0.235 \pm 0.001) \text{ cm}, \\
 \text{drift chamber 1 absolute position} &= (0.62 \pm 0.01) \text{ cm}, \\
 \text{drift chamber 2 absolute position} &= (0.76 \pm 0.01) \text{ cm}, \\
 \text{drift chamber angle} &= (0.045 \pm 0.005) \text{ deg}.
 \end{aligned} \tag{4.9}$$

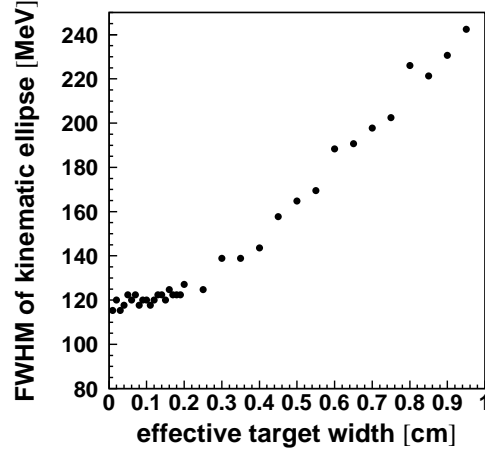


Figure 4.13: Simulated dependence of the distribution width (FWHM) of the projection along the kinematic ellipse on the effective target width.

The obtained target position and effective size are in the good agreement with the values derived from the measurement with the diagnosis tool.

### 4.3.3 Density distribution of the cluster target stream

Figure 4.14 shows the changes of the average distance between the theoretical ellipse and the experimental distribution as a function of time. These variations correspond to changes of the centre of the density distribution of the target and hence influence the resolution of the missing mass. As an example of the effect, the missing mass spectra for the  $pp \rightarrow ppX$  reaction obtained for the first and second half of the measurement at 3211 MeV/c momentum are presented in Figure 4.15, where the first part of the measurement (from  $\sim 100$  h to  $\sim 175$  h) corresponds to the large variation of the kinematic ellipse position, while the second part (from  $\sim 175$  h to  $\sim 250$  h) to the small variations. The presented spectra differ and the  $\eta'$  signal is better visible in the data collected in the period with smaller variations (a detailed description of the missing mass technique will be presented in section 5.3). Such fluctuations could be explained by variations of the beam momentum due to the changes of the beam optics<sup>7</sup> or by small fluctuations of the density distribution of the target stream. However, the beam optics variation is excluded by the results of the monitoring of the stability of the COSY beam (as described in the next section). The observed variations of the kinematic ellipse position can be plausibly explained by density changes inside the target stream in beam direction. In this direction the target length is about 1 cm (see section 4.3.1) and expected fluctuations of the density can cause the changes of the centre of the target stream distribution in the order of 1 mm. Such variations along the z-axis were observed by

<sup>7</sup>The variations of the beam optics could be caused by e.g. the variations of the dipole currents, or small deformation of the dipole shape caused by temperature changes.

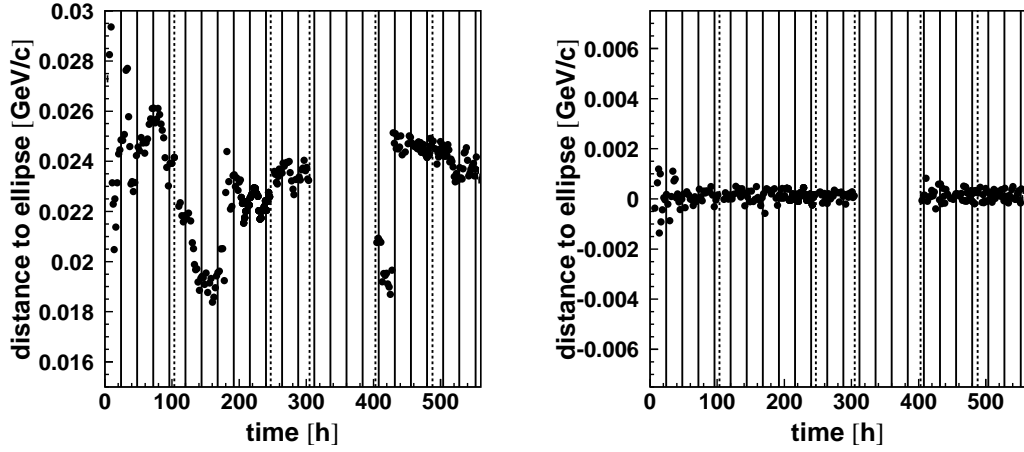


Figure 4.14: **Left:** Distance between the theoretical ellipse and the experimental distribution for the elastic kinematics plotted as a function of time. Points denote results averaged over  $\sim 2$  hours. Solid lines denote succeeding days of the measurement, while the dashed lines separate periods with different beam momenta (3218, 3211, 3214, 3213 and 3224 MeV/c). The values are not around 0 since at this stage the analysis was performed without corrections for the target and drift chamber positions as described in the previous section. The four days gap after  $\sim 300$  hour of measurement time is due to a cyclotron down time. **Right:** The same data as presented on the left plot but analysed after correction of the changes of the centre of the density inside the target stream (see text for the details). Both plots have the same scale on the vertical axis.

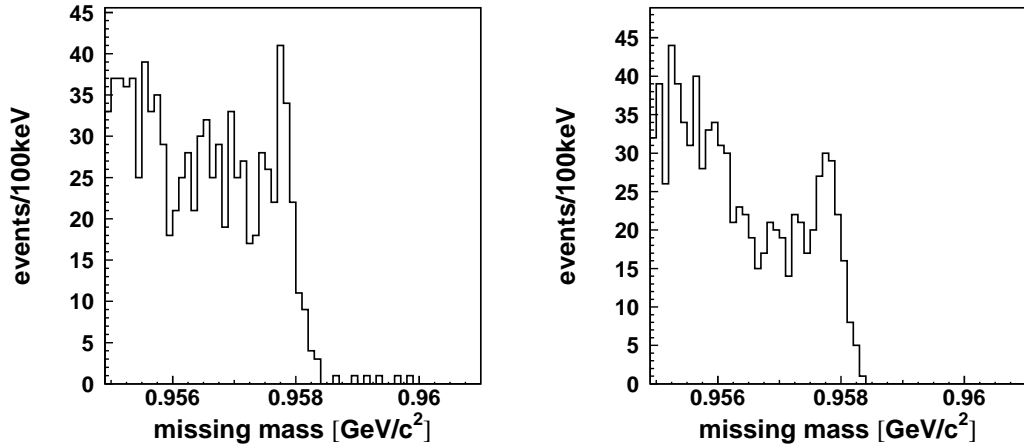


Figure 4.15: Missing mass spectra extracted from data collected for 3211 MeV/c beam momentum. **Left:** Result from  $\sim 100$  h to  $\sim 175$  h of the experiment. **Right:** Result from  $\sim 175$  h to  $\sim 250$  h of the experiment.

means of the diagnosis unit as mentioned in Section 4.3.1. Therefore, in the following analysis we assumed that the observed deviations are due to the target density variations and corrected them by continuous changes of the nominal value of the centre of the target along the  $z$  direction (see Figure 4.16). The corrections were interpolated between points calculated for each  $\sim 2$  hours interval of beam time. The average distance to the expected kinematic ellipse after the correction for target density fluctuation is presented in the right panel in Figure 4.14. The first two days of the measurement were used for different test of the detection system and the optimisation of the beam optics which cause somewhat larger fluctuations during this period. Therefore the data collected during those two days were not used for the final  $\Gamma_{\eta'}$  determination.

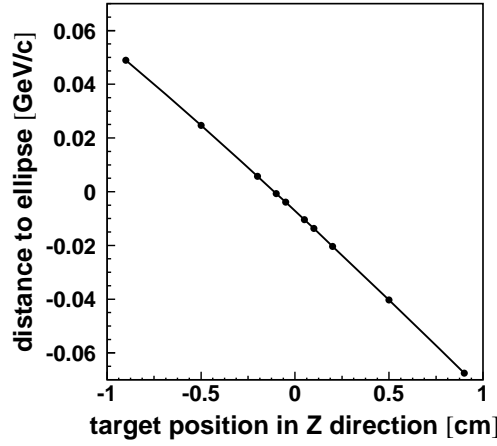


Figure 4.16: Average deviation of the experimental points distribution from the expected kinematic ellipse as a function of target position in the direction parallel to the COSY beam.

## 4.4 Monitoring of the stability of the proton beam

Although the frequency of the circulating beam is monitored routinely several times per minute, during the described experiment a measurements of additional parameters were performed in order to provide a better control of the stability of the proton beam.

### 4.4.1 Synchrotron parameters

The standard technique for monitoring the beam momentum at the COSY accelerator is the measurement of the frequency distribution of the circulating beam. Based on the

equation [52, 70, 71]:

$$\frac{f - f_0}{f_0} = \eta_{beam} \frac{p - p_0}{p_0}, \quad (4.10)$$

where  $f$  denotes the frequency and  $p$  denotes the beam momentum, ( $f_0$  and  $p_0$  correspond to their nominal values, respectively) one can transform the frequency into the beam momentum. (The determination of the real value of the beam momentum is described in section 5.4.) The  $\eta_{beam}$  parameter depends on the settings of the accelerator and for the described measurement was equal to  $-0.10 \pm 0.01$  [70]. As an example a spectrum transformed to the momentum coordinate for the lowest beam energy used in the experiment is presented in Figure 4.17. The beam momentum distribution is smooth and its spread is equal to 2.5 MeV/c (FWHM). However, due to the position of the COSY-11 target system in a bending section of the COSY ring in a dispersive region, the effective spread of the beam (the momentum range *seen* by target) is smaller. The dispersion relation is:

$$\Delta x = D \frac{\Delta p}{p_0}, \quad (4.11)$$

where  $\Delta x$  and  $\Delta p$  denote the difference between the real and nominal values of particle orbit and momentum, respectively. The dispersion in the COSY-11 target system was set to  $D = 14.15 \text{ m}$ , which (taking into account the 1.06 mm effective target width) results in an effective beam spread of  $\pm 0.06 \text{ MeV/c}$ . The relevant momentum range is marked by blue lines in Figure 4.17.

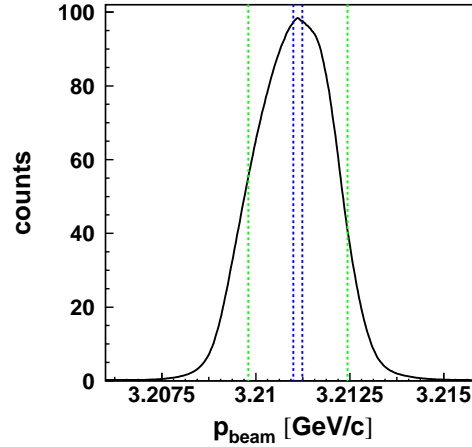


Figure 4.17: Example of the momentum spectrum for the measurement with the nominal beam momentum of 3211 MeV/c. The dashed lines limit the effective spread of the beam due to the dispersion relation for a target width of 1 mm (blue) and 1 cm (green).

After variations of the position of the kinematic ellipse have been observed during an *on-line* analysis, measurements of additional (to the frequency spectrum) parameters were implemented. To check the stability of the beam optics the current through

the dipole magnets was controlled, however, no fluctuations on the level of  $10^{-5}$  during beam cycles were found. Furthermore the temperatures of the incoming and outgoing water used for the magnets cooling were monitored<sup>8</sup> – also without any correlations with the observed behaviour of the ellipse position.

#### 4.4.2 Atmospheric conditions

In addition to the control of the hardware status, the atmospheric conditions were monitored inside and outside the COSY-tunnel. Thermograph and hygograph were installed in the COSY tunnel close to the COSY-11 detector and information about air temperature, pressure and humidity outside the building were delivered by the meteorology station (courtesy of Dr. Axel Knaps). No correlations to the observed behaviour of the kinematic ellipse was found.

The stability of the parameters described in this and the previous sections raised our confidence that the fluctuations of the kinematic ellipse position was due to the density fluctuation inside the target stream.

---

<sup>8</sup>The variation of the temperature could cause changes of the dipole dimensions and hence changes of the magnetic field *shape*.



# Chapter 5

## Identification of the $pp \rightarrow pp\eta'$ reaction

The identification of protons via the invariant mass method and the determination of missing masses of unregistered particles allow to select  $pp \rightarrow pp\eta'$  events.

### 5.1 Identification of the outgoing protons

The invariant mass of registered particles was calculated from the equation:

$$m_{\text{inv}}^2 = \frac{p^2(1 - \beta^2)}{\beta^2}, \quad (5.1)$$

where momentum  $p$  and velocity  $\beta$  of the particle were determined by means of drift chambers (track reconstruction through the known magnetic field) and the S1-S3 hodoscope (ToF), respectively. The correlations of the two invariant masses for events with two reconstructed tracks are presented in Figure 5.1. Appropriately chosen cuts allow to select events corresponding only to two registered protons.

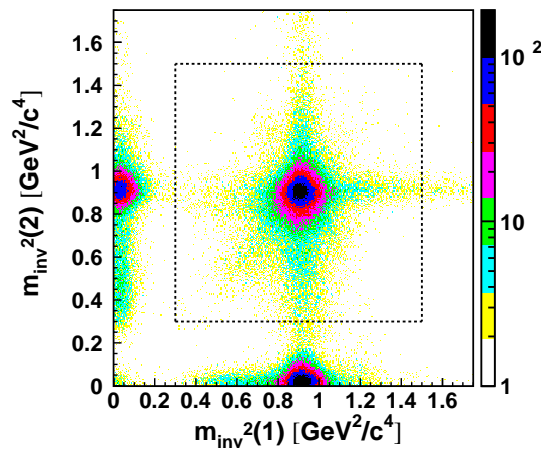


Figure 5.1: Distribution of the invariant mass of two registered particles. The superimposed black dashed square represents the applied cut. Outside the selected area  $\pi^+p$  and  $p\pi^+$  events are visible. Note that the number of entries is given in the logarithmic scale.

## 5.2 Determination of the relative beam momenta

Due to the inaccuracy of the orbit length [70], the COSY crew can set the absolute momentum of the beam (nominal value) only with an accuracy of 3 MeV/c. Since this was not sufficient for our experiment, we decided to use collected  $pp \rightarrow pp\eta'$  and  $pp \rightarrow pp$  events for the determination of the absolute beam momenta. Based on the position of the  $\eta'$  signals in the missing mass spectra the absolute beam momenta can be derived. For this procedure the mass of the  $\eta'$  meson has to be determined as will be discussed later. Since, on the other hand, the correct signal position can be obtained only for a background-free missing mass spectrum, the background has to be subtracted first. The method used for the background subtraction (see the next section) requires information about the relative beam momenta, which can be determined by the comparison of kinematic ellipses from  $pp \rightarrow pp$  events (see Section 4.3.2). Although the position of the kinematic ellipse depends stronger on the target position than on the beam momentum (see Section 4.3.2) it can be used for calculations of the relative beam momenta, since the fluctuations during the measurement were corrected before. As a result we obtained the following momenta relative to the lowest measured one:

$$\begin{aligned}\Delta p_{1-2} &= 1.85 \pm 0.01 \text{ MeV/c} \\ \Delta p_{1-3} &= 2.82 \pm 0.01 \text{ MeV/c} \\ \Delta p_{1-4} &= 6.53 \pm 0.01 \text{ MeV/c} \\ \Delta p_{1-5} &= 12.66 \pm 0.01 \text{ MeV/c}\end{aligned}$$

## 5.3 Missing mass spectra and background subtraction

The determined missing mass spectra of the five measured energies were used (i) to determine the background, (ii) to evaluate the absolute beam momenta and (iii) to calculate the width of the  $\eta'$  meson (see next chapter).

### 5.3.1 Experimental background from different energies

The missing mass spectrum of the multipion background can be established either by Monte Carlo simulations (see e.g. [60]) or by the usage of the experimental background collected for another energy [72]. The second method was used in the analysis and is described in this dissertation, since it allows to avoid additional approximations and assumptions.

The used background subtraction method was described in detail in article [72]. It is based on the observation that the shape of the multipion mass distribution does not change when the excess energy for the  $pp \rightarrow pp\eta'$  reaction varies by a few MeV only

since the dominant background originates from  $2\pi$  and  $3\pi$  production [40] and the excess energy for either of these reactions is larger than 0.5 GeV. Figure 5.2 demonstrates that the change in the shape of the missing mass distributions is in the order of 1% over a range more than 0.2 GeV and in this experiment a range of about 0.005 GeV is important. From the measurement below the threshold for the  $\eta'$  production, the signal-free background can be obtained and used for the close-to-threshold production process. Also the measurements sufficiently high above the threshold, with an excess energy larger than the resolution of the missing mass determination, provides a signal-free background for close-to-threshold production data.

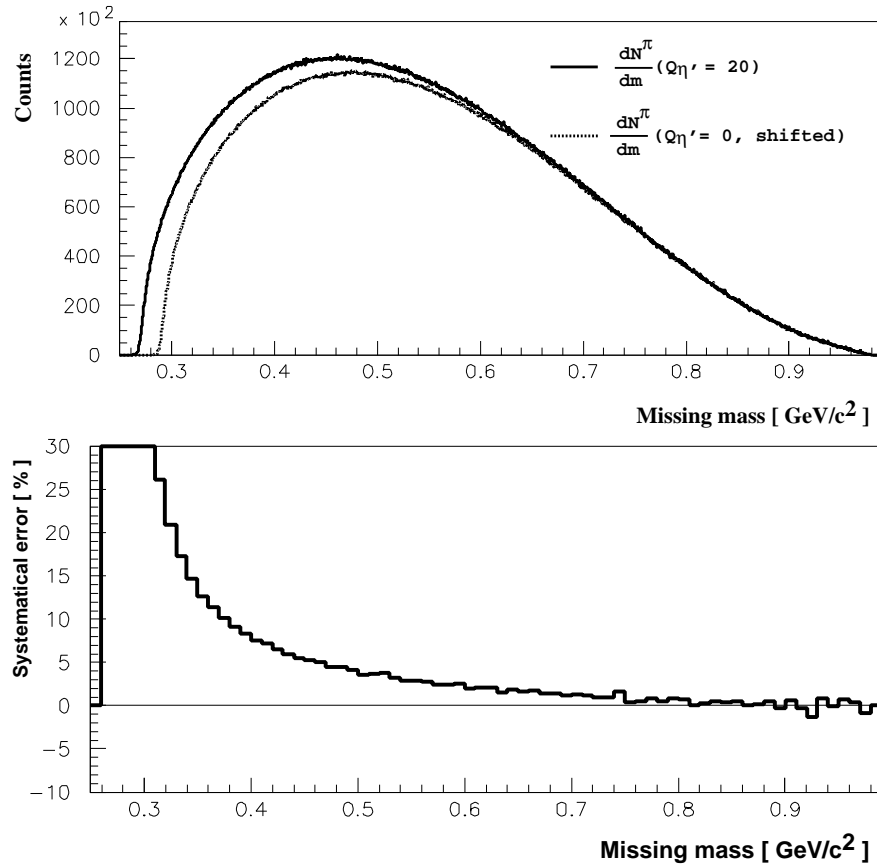


Figure 5.2: **Upper:** Missing mass distribution with respect to the  $pn$  system calculated from Monte Carlo data for the  $pn \rightarrow pn\pi\pi$  process for a beam momentum at the threshold (dotted line) and 20 MeV above the threshold for the  $pn \rightarrow pn\eta'$  reaction (solid line). The dotted histogram was shifted by 20 MeV. **Lower:** Difference between the spectra in the upper plot normalised to the solid line, which gives the systematical error due to the background determination. The plots are adapted from [72].

The excess energy in the centre of mass system (CM) is defined as:

$$Q = \sqrt{s} - \sum_i^N m_i, \quad (5.2)$$

where  $\sqrt{s}$  denotes the centre-of-mass total energy of the colliding protons system and  $N$  is the number of outgoing particles. In order to determine the background shift between the spectra the relative values of  $Q$  have to be known. Since  $Q$  depends inter alia on the beam momentum from which the relative changes can be controlled via the position of the experimental distributions of the kinematic ellipse, relative  $Q$  values can be obtained. Missing mass spectra for the  $pp \rightarrow ppX$  reaction obtained for the lowest (3211 MeV/c) and highest (3224 MeV/c) beam momenta in the described experiment are presented in Figure 5.3. It is important to stress that the background distribution is smooth in the whole range studied. The spectrum for the beam momentum of 3224 MeV/c was shifted according to the described method and normalised to the data from lower energy. As one can see the background shape in the signal-free region is the same with respect to the statistical errors for both energies. This confirms the correctness of the above described method for background determination.

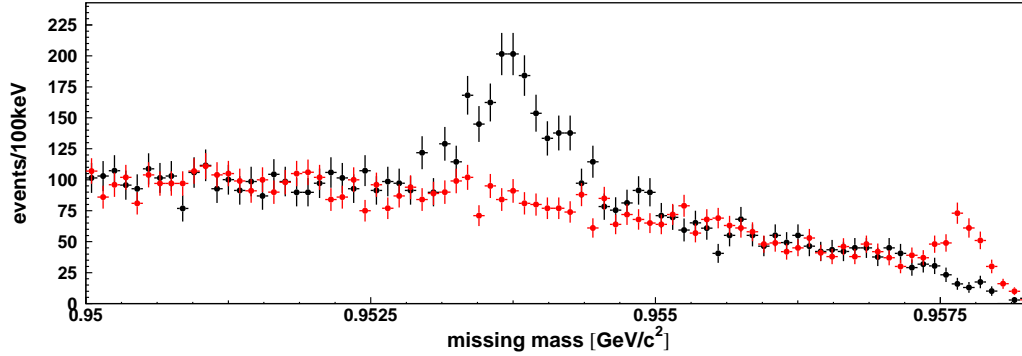


Figure 5.3: Missing mass spectra for the  $pp \rightarrow ppX$  reaction. Red points correspond to the measurement at 3211 MeV/c beam momentum (the lowest one in the described experiment), while black ones represent the measurement at the highest beam momentum (3224 MeV/c). The black points were shifted by the difference between the kinematic limits and normalised to the red points (see text for details).

### 5.3.2 Background parametrisation with polynomial fit

To decrease the influence of the statistical fluctuation of the background and based on the smooth change of the background in the signal region (see Figure 5.3) the background for each energy was determined as a second order polynomial which was de-

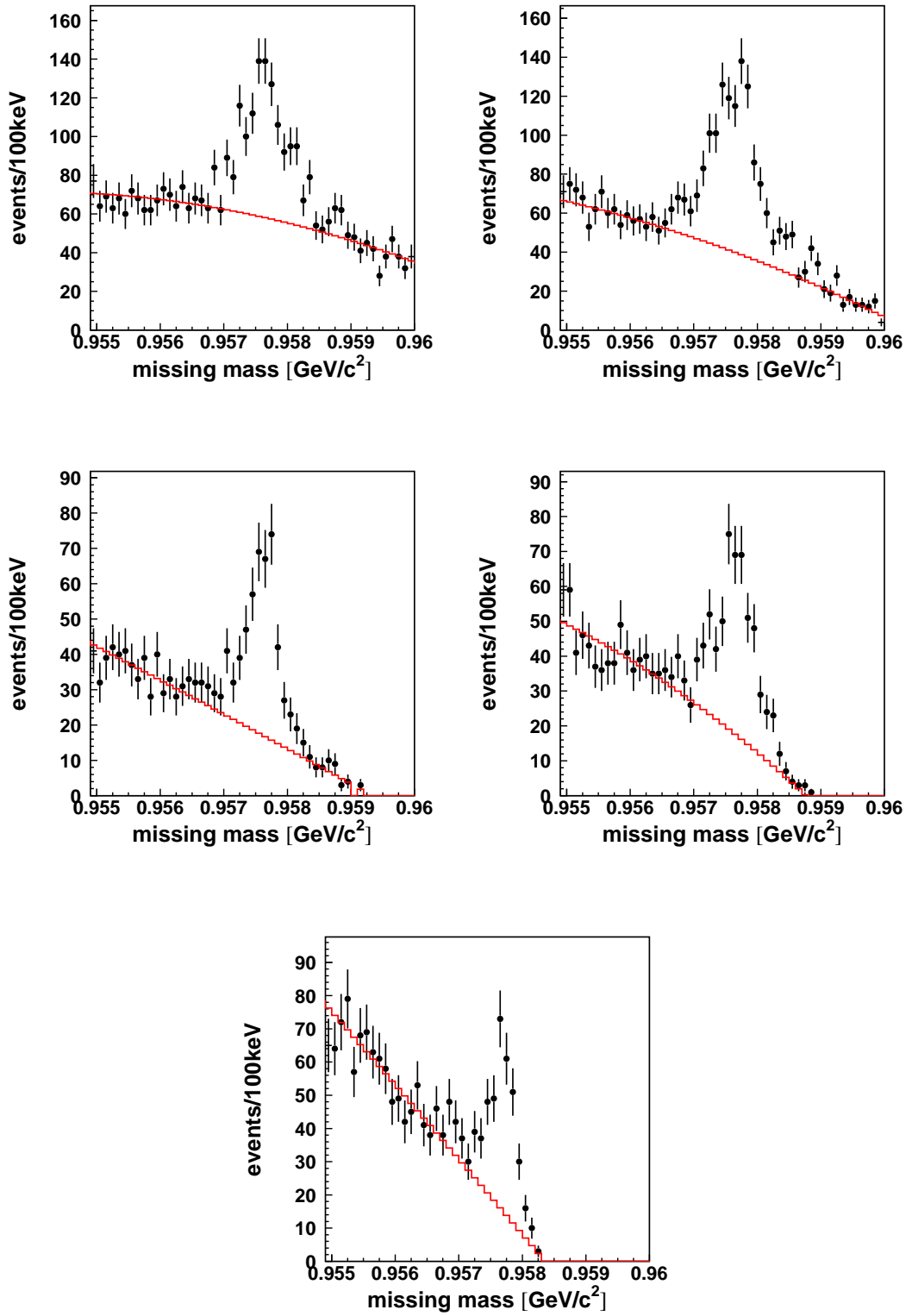


Figure 5.4: Missing mass spectra for the  $pp \rightarrow ppX$  reaction obtained for the beam momenta of 3224, 3218, 3214, 3213 and 3211 MeV/c (from left to right, top to bottom). The black points represent the experimental data, while the red curves are the shifted and normalised second order polynomials obtained from the fit to the background (for the description see text).

rived from data at a different energy and was shifted and normalised to the actual data. The full procedure for background determination consists of the following steps:

1. fit of a second order polynomial to the missing mass spectrum in the signal-free region for a lower/higher beam energy;
2. shift of the obtained curve according to the calculated Q difference;
3. normalisation of the curve to the data obtained for the actual beam energy.

The results are presented in Figure 5.4. The determined curves agree well with the background data within the statistical accuracy.

## 5.4 Absolute beam momentum determination

The knowledge of the relative beam momenta (see Section 5.2) and the background shape (see previous section) allows to determine the absolute beam momenta based on the position of the  $\eta'$  signal. The procedure relies on the comparison of the position of the  $\eta'$  signal with the  $\eta'$  mass<sup>1</sup>. Due to the best signal-to-background ratio and the sharpest signal, for the derivation of the absolute value of Q, the missing mass obtained for the lowest beam momentum was used, while the other four beam momenta were adjusted with respect to the relative differences obtained in Section 5.2. Table 5.1 presents the values of the nominal and real beam momenta and corresponding real Q values. For all measurements the real beam momentum is lower by about 0.5 MeV/c.

beam momentum [MeV/c]		real excess energy [MeV/c <sup>2</sup> ]
nominal	real	
3211	3210.7	0.8
3213	3212.6	1.4
3214	3213.5	1.7
3218	3217.2	2.8
3224	3223.4	4.8

Table 5.1: Nominal and real beam momenta for the measurement of the  $pp \rightarrow pp\eta'$  reaction and corresponding real values of excess energy.

The accuracy of the real beam momentum derivation depends on the accuracy of both the knowledge of the  $\eta'$  mass as well as determination of the relative beam momenta. The first component is of systematic type and contributes as an error of  $\pm 0.2$  MeV/c whereas the second one is of statistical nature and its contribution is negligibly small.

---

<sup>1</sup> $m_{\eta'} = (957.78 \pm 0.06) \text{ MeV}/c^2$  [3]

The systematically lower value of the real beam momentum of about 0.5 MeV/c matches well with the range of accuracy in beam momentum setup being typically  $\pm 3$  MeV/c [70] and the results are in line with previous experiences at COSY where also the real beam momentum was smaller than the nominal one [63, 73].





## Chapter 6

### Determination of the total width

The determination of the total width of the  $\eta'$  meson was based on the simultaneous comparison of all experimental missing mass spectra with the Monte Carlo generated ones, where  $\Gamma_{\eta'}$  was varied in the range from 0.14 to 0.38 MeV.

#### 6.1 Comparison of experimental data with simulations

The  $pp \rightarrow pp\eta'$  reaction and trajectories of the outgoing protons were simulated and detector signals were generated by the GEANT3-based program [74] for the five investigated beam energies. The program itself contains the implementation of the whole geometry of the COSY-11 detector setup. It takes into account also known physical processes like multiple scattering and nuclear reactions in the detector material, as well as the detector and target properties established and described in the previous chapters, like: position and spatial resolution of the drift chambers, size and position of the target stream and value and spread of the beam momentum.

Afterwards the generated events were analysed in the same way as the experimental data and sets of missing mass spectra for the five measured energies were obtained for the values of  $\Gamma_{\eta'}$  ranging from 0.14 to 0.38 MeV. For simulations of the mass distribution of the  $\eta'$  meson the Breit-Wigner formula was used. Finally the Monte Carlo missing mass spectra with an  $\eta'$  signal were added to the second order polynomial fitted to the experimental backgrounds (see Section 5.3.2). The obtained spectra were compared to the experimental ones via calculating the  $\chi^2$  derived from the maximum likelihood method [75, 76]. The following formula was used for the  $\chi^2$  computation:

$$\chi^2 = 2 \sum_{i=1}^K \left[ \alpha N_i^{\text{MC}} + B_i - N_i^{\text{exp}} + N_i^{\text{exp}} \ln \left( \frac{N_i^{\text{exp}}}{N_i^{\text{MC}} + B_i} \right) \right], \quad (6.1)$$

where  $K$  denotes the number of bins in the range where the histograms were compared,  $\alpha$  is the free parameter of the fit which describes the normalisation factor of the Monte

Carlo spectra with the  $\eta'$  signal. The numbers of entries in the  $i$ -th bin in the Monte Carlo spectra, the background and the experimental spectra are denoted as  $N_i^{\text{MC}}$ ,  $B_i$  and  $N_i^{\text{exp}}$ , respectively. The dependence of the calculated  $\chi^2$  – quantifying a difference between the experimental and Monte Carlo spectra – on the applied  $\Gamma_{\eta'}$  value is presented in Figure 6.1. The minimum value of  $\chi^2$  corresponds to  $\Gamma_{\eta'} = 0.226$  MeV, which is the most likely value of the total width of the  $\eta'$  meson. The right plot in Figure 6.1 is the close-up of the left plot in the region of the minimum, where the range of the horizontal axis corresponds to the range where  $\chi^2$  differs by one with respect to its minimum value. Since the calculated value of  $\chi^2$  is not normalised to the number of degrees of freedom, the range of  $\Gamma_{\eta'}$  where  $\chi^2 = \chi_{\min}^2 + 1$  corresponds to the statistical error of the measurement [1, 3, 77], which in case of the reported measurement is  $\pm 0.017$  MeV. The experimental spectra of the missing mass superimposed with the sum of the background polynomial and the Monte Carlo generated signals for  $\Gamma_{\eta'} = 0.226$  MeV/c are presented in Figure 6.2. The blue dashed lines mark the range where the experimental histograms were compared to the result of the simulations. The presented missing mass signals are the convolution of the total width of the  $\eta'$  meson and the experimental resolution.

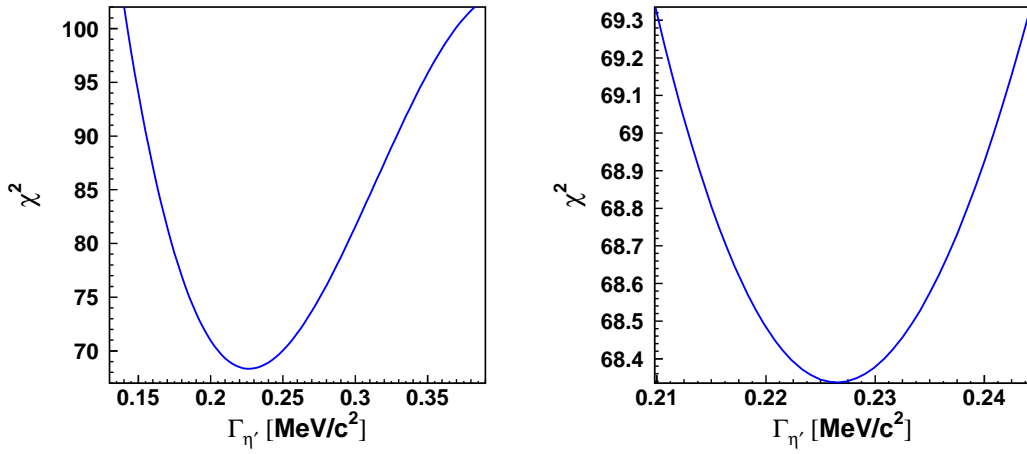


Figure 6.1: **Left:** Similarity (as a value of  $\chi^2$ ) of the missing mass spectra obtained from the measurement and from Monte Carlo simulations. The minimum value corresponds to  $\Gamma_{\eta'} = 0.226$  MeV. **Right:** Close-up of the left plot with the range where  $\chi^2 = \chi_{\min}^2 + 1$ , which corresponds to the value of the statistical error of the measurement.

The observed dependence of the width of the missing mass signals on the excess energy (see Figure 6.2 and 6.3) is due to the propagation of errors of protons momenta involved in the missing mass calculations [49]. Since the Monte Carlo program is re-

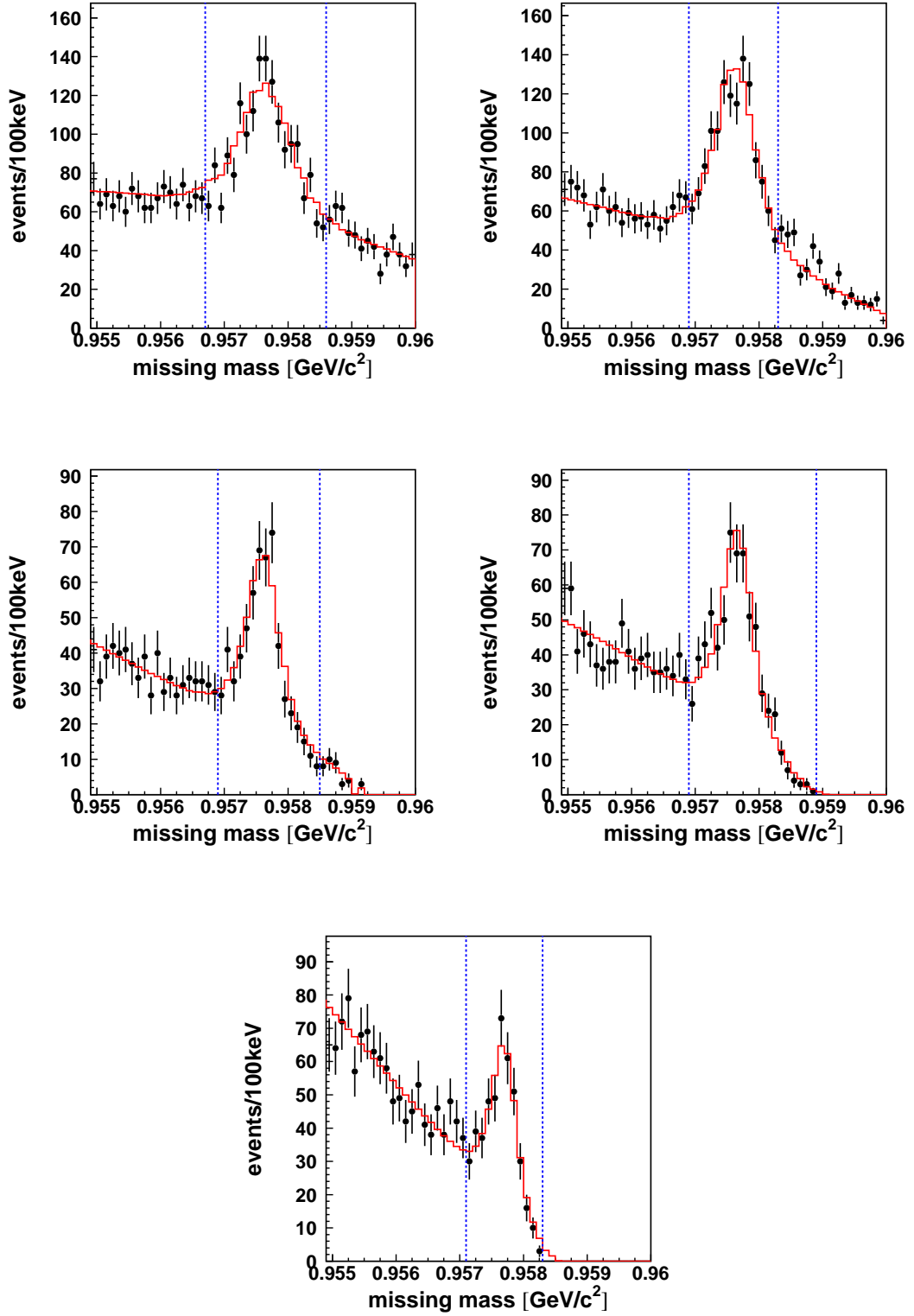


Figure 6.2: The missing mass spectra for the  $pp \rightarrow ppX$  reaction for excess energies in the CM system equal to 4.8, 2.8, 1.7, 1.4, and 0.8 MeV (from left to right, top to bottom). The  $\eta'$  meson signal is clearly visible. The experimental data are presented as black points, while in each plot the red line corresponds to the sum of the Monte Carlo generated signal for  $\Gamma_{\eta'} = 0.226$  MeV and the shifted and normalised second order polynomial obtained as a fit to the signal-free background region for another energy.

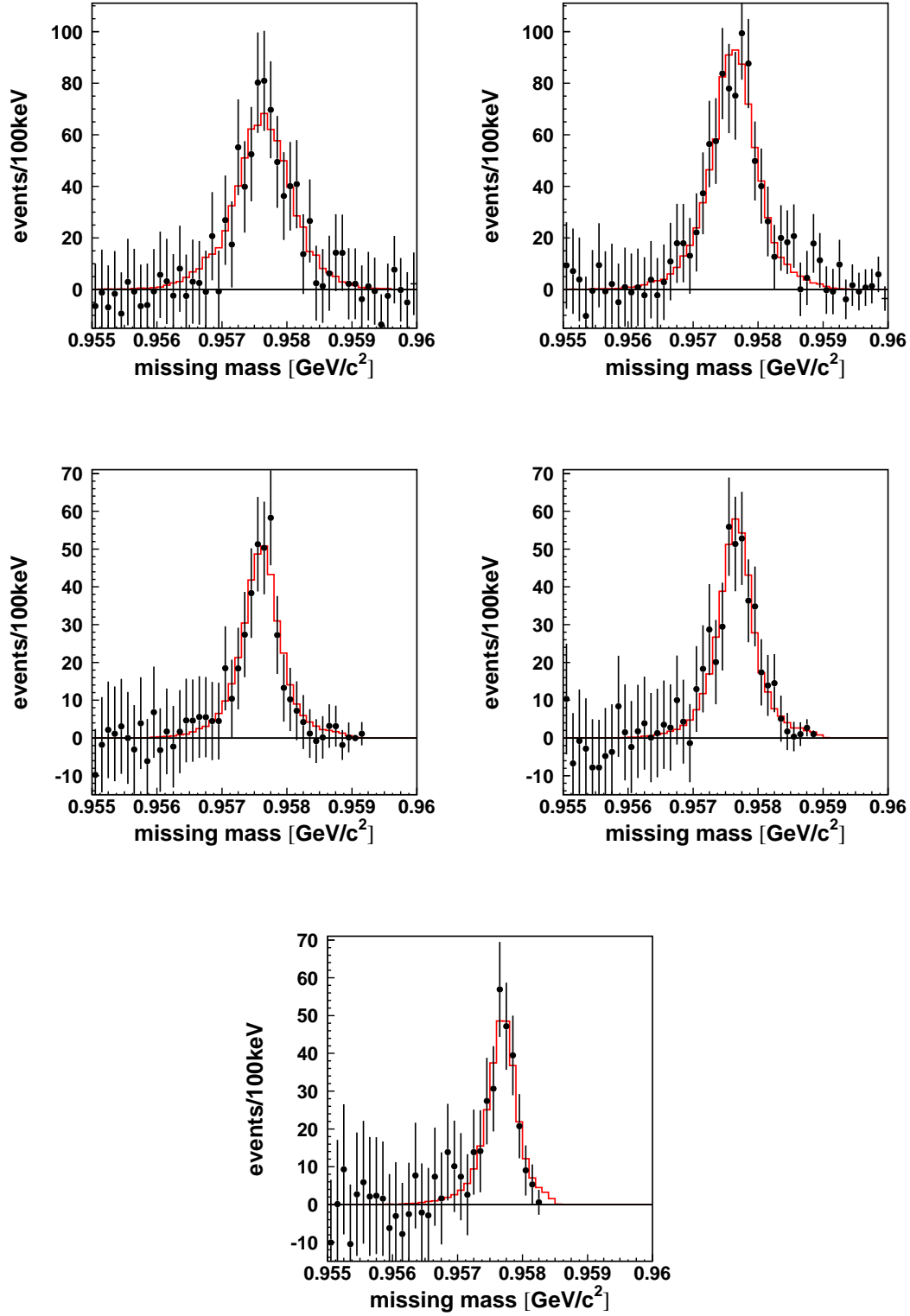


Figure 6.3: Background-free missing mass spectra for the  $pp \rightarrow ppX$  reaction for excess energies 4.8, 2.8, 1.7, 1.4, and 0.8 MeV (from left to right, top to bottom) in CM system. The experimental data are presented as black points, while the red lines correspond to the Monte Carlo generated signal for  $\Gamma_{\eta'} = 0.226$  MeV.

producing the changes of the experimental spectra with energy very well, this confirms the correctness of the established detector and target characteristics.

For completeness the experimental missing mass spectra for the  $pp \rightarrow ppX$  reaction after background subtraction are presented in Figure 6.3. More than 2300  $\eta'$  mesons were reconstructed and achieved experimental mass resolution for the lowest measured energy amounts to  $\text{FWHM} = (\text{FWHM}_{\text{missing mass}}^2 - \Gamma_{\eta'}^2)^{1/2} = 0.33 \text{ MeV}/c^2$ .

## 6.2 Systematic error estimation

The accuracy of the determination of collected in Table 6.1 parameters of the COSY-11 detector and the COSY accelerator contribute to the systematic error of the derivation of the  $\eta'$  width. The estimated values of the influence of the accuracy of each parameter on the final result are presented. The contributions from the accuracy of the target position and size, the map of the magnetic field, the position of the drift chambers and the absolute beam momentum determination were estimated as the difference between the derived result of the  $\Gamma_{\eta'}$  and the  $\Gamma_{\eta'}$  values established by changing particular parameter by its error value. The systematic error due to the method of the background

parameter	contribution to the systematic error [MeV]
map of the magnetic field	0.007
target position	0.006
background subtraction method	0.006
ranges of missing mass spectra, where $\chi^2$ was calculated	0.005
bins width	0.004
absolute beam momentum	0.003
final state interaction (FSI) between protons	0.003
effective target width	0.002
position and orientation of the drift chambers	0.001

Table 6.1: Summary of the parameters contributing to the systematic error of the  $\Gamma_{\eta'}$  measurement at the COSY-11 detector.

subtraction was established as the difference between  $\Gamma_{\eta'}$  values determined using experimental background shapes from different energies<sup>1</sup>. The bin width was changed from 0.1 to 0.04 MeV/ $c^2$ , while the ranges of the missing mass spectra, where  $\chi^2$  was

<sup>1</sup>For a missing mass spectrum at a given energy each of four remaining spectra could be used for the background determination.

calculated, were enlarged by  $0.7 \text{ MeV}/c^2$  at each side (which corresponds to seven bins in plot 6.2). The estimation of the influence of the final state protons-proton interaction is very conservative. The reported value is the difference between the case where the FSI was and was not taken into account [78, 79].

The total systematic error was calculated as a square root of the sum of the squared values listed in Table 6.1 and the final result of the measurement of the total width of the  $\eta'$  meson conducted with the COSY-11 detector is  $\Gamma_{\eta'} = 0.226 \pm 0.017(\text{stat.}) \pm 0.014(\text{syst.}) \text{ MeV}$ .

# Chapter 7

## Summary

The aim of this work was to determine the total width of the  $\eta'$  meson with a unique precision and independently of the other properties of this meson, like e.g. partial widths or production cross sections. The motivation for the measurement of the total width of the  $\eta'$  meson as well as the experimental method and the final result have been presented.

The value of  $\Gamma_{\eta'}$  was established directly from the measurement of the mass distribution of the  $\eta'$  meson. The  $\eta'$  meson was produced in proton-proton collisions via the  $pp \rightarrow pp\eta'$  reaction and its mass was reconstructed based on the information about the momentum vectors of the protons before and after the reaction. The experiment was conducted in the Research Centre Jülich in Germany. The accelerated and stored protons were circulating through the stream of the hydrogen cluster target in the ring of the cooler synchrotron COSY. The two outgoing protons were measured by means of the COSY-11 detector. The reconstruction of a particle trajectory through the known magnetic field allows for the momentum determination, while the ToF method provides information about the velocity. The identification of the particle is an outcome of the combination of those two informations, while the  $pp \rightarrow pp\eta'$  reaction was identified via the missing mass technique. Altogether more than 2300  $pp \rightarrow pp\eta'$  events were reconstructed. The comparison of the derived experimental missing mass spectra with Monte Carlo generated ones results in a  $\chi^2$  dependence on the  $\Gamma_{\eta'}$  value used in the simulation.

The statistical error of the final result was obtained directly from a  $\chi^2$  vs  $\Gamma_{\eta'}$  plot at  $\chi^2 = \chi^2_{min} + 1$  value [1, 3, 77]. A small systematic error of the final result was achieved due to:

- the excellent properties of the stochastically cooled proton beam;
- the application of a decreased size of the target stream which resulted in a small beam momentum spread and a small geometrical size of the reaction region;

- monitoring of the properties of the reaction region by two independent methods: by a specially developed diagnosis unit and by examining of the momentum distributions of the elastically scattered protons;
- the close-to-threshold measurement – where  $\partial(mm)/\partial p$  approaches zero.
- the verification of the characteristics of the synchrotron beam, target stream and detector setup by a comparison of the results obtained for five different beam momenta.

The value of  $\Gamma_{\eta'} = 0.226 \pm 0.017(\text{stat.}) \pm 0.014(\text{syst.})$  MeV determined in the analysis described in this dissertation is three times more precise than the best classified measurement until now ( $\Gamma_{\eta'} = 0.28 \pm 0.10$  MeV) [1] and the achieved accuracy is in the same order as the value obtained by the PDG from a fit to 51 measurements of branching ratios ( $\Gamma_{\eta'} = 0.204 \pm 0.015$  MeV) [3]. It is also important to note that the achieved mass resolution amounts to  $\text{FWHM} = 0.33 \text{ MeV}/c^2$  and is of the same order as the total width of the  $\eta'$  meson itself, which excludes the possibility of a multistructure in the  $\eta'$  signal at this level.

The value of the  $\eta'$  meson total width recommended by Particle Data Group [3] is correlated with the partial width for the  $\eta' \rightarrow \gamma\gamma$  decay [4], while the average of two available measurements [1, 2] has an 30% error. The result of the measurement and analysis presented in this dissertation has an accuracy of 13% and agrees within the error bars with the value provided by the PDG fit, however, the value established in this work is independent of any of the branching ratios and the  $\Gamma(\eta' \rightarrow \gamma\gamma)$  measurements. Therefore, it can be used as a *tool* to translate branching ratios to partial widths and vice versa, and applied for the investigations of e.g. the gluonium component in the  $\eta'$  meson [20, 22] and, indirectly, for studies of the quark mass difference  $m_d - m_u$  [25–27].

This was the last measurement conducted by the COSY-11 group. It therefore could take advantage of the methods developed in the course of the nearly eleven years of experiments [80], which, as shown in this work, resulted in the unique mass resolution.



*The journey is the reward.*  
Chinese Proverb



## Acknowledgements

The list of people who contributed into this work is too long to be written in a short note. I would like to thank all of you for your indispensable help during the preparation of this thesis. In particular those of you who are not mentioned by name – thank you.

Especially I would like to express my gratitude to my supervisor Prof. Paweł Moskal, a man who gave me an opportunity for better understanding of experimental physics, for his suggestions, advices and patience. I would like to thank you, Paweł, for possibility to work together during all of these years, although this work was rather an adventure than obligation. All of our discussions were great pleasure for me. Thank you.

In addition I would like to thank to:

- Prof. Bogusław Kamys for discussion and suggestions concerning this work and for support during the period of studies;
- Prof. James Ritman for his outstanding support during my stay in the Research Centre Jülich and constructive advices and comments during presentations of the analysis progress;
- Prof. Walter Oelert for the corrections of this dissertation and help since my very first visit in Jülich;
- Dr Dieter Grzonka for the suggestions and help during all of the stages of the data analysis, for developing the diagnosis unit, which allowed us to achieve unique precision of the measurement, and also for the corrections of this dissertation;
- Dr Thomas Sefzick for all his help during my work, for the corrections of this thesis and for very fast arrangement of the hygograph and thermograph during the beam time;
- Prof. Jerzy Smyrski for the discussions concerning the properties of drift chambers and for the corrections of this work;
- Dr Magnus Wolke for the time spent on explanations of the acquisition and coding of the data at COSY-11 system;
- Alexander Täschner for taking care of the COSY-11 target setup during the experiment and for the tests and developing of the new collimator with rectangular opening;
- Dr Peter Wüstner for always fast reactions in case of problems with the Alpha machines;
- the COSY team for providing a good quality beam during the experiment;
- the reviewers, Prof. Agnieszka Zalewska and Dr hab. Tomasz Kozik, for agreeing to devote their time to reference this dissertation;
- Prof. Lucjan Jarczyk for all his comments, questions and provoked discussions about the  $\eta'$  meson and data analysis;

- Dr Rafał Czyżykiewicz for the corrections of this dissertations and many, many discussions which reach behind the horizon, also for the chess and volleyball games;
- Adrian Dybczak for the discussions and collective studies during all the time spent in Cracow;
- Wojciech Krzemiń for the answers to the not so trivial questions and all the discussions on the IKP corridor;
- Cezary Piskor-Ignatowicz for putting me in touch with Paweł Moskal and for very deep and serious discussions;
- Dagmara Rozpędzik and Wojciech Bruzda for the support in the typical PhD student problems;
- Małgorzata Hodana and Benedykt Jany for all the movie evenings in Jülich;
- Barbara Rejdych-Iwanek, Michał Silarski, Joanna and Paweł Klaja, Jarosław Zdebik, Marcin Zieliński and Michał Janusz for a nice atmosphere of work;
- Małgorzata Fidelus, Izabela Ciepał, Borys Piskor-Ignatowicz and Rafał Sworst for the working climate in room 03a.

Finally, I am indebted to my beloved Alina Ptaszek for her support, understanding and patience.

Last but not least I would like to say thank you to my Parents: Dziękuję Wam, Mamo i Tato, za pomoc i wsparcie na wszystkich drogach, którymi kroczyłem.

# Bibliography

- [1] D. M. Binnie et al., *Phys. Lett.* **B83**, 141 (1979). 1, 4, 5, 7, 46, 51, 52
- [2] R. Wurzinger et al., *Phys. Lett.* **B374**, 283–288 (1996). 1, 4, 5, 7, 52
- [3] C. Amsler et al., *Phys. Lett.* **B667**, 1 (2008). 1, 4, 5, 7, 42, 46, 51, 52
- [4] B. Di Micco, *Acta. Phys. Pol. Supp.* **B2**, 63–70 (2009). 1, 3, 4, 52
- [5] B. Borasoy and R. Nissler, *AIP Conf. Proc.* **950**, 180–187 (2007). 1, 4
- [6] E. Czerwiński, D. Grzonka, and P. Moskal, *COSY proposal* 31 I/2006 (2006). 2
- [7] G. R. Kalbfleisch et al., *Phys. Rev. Lett.* **12**, 527–530 (1964). 3
- [8] M. Goldberg et al., *Phys. Rev. Lett.* **12**, 546–550 (1964). 3
- [9] P. M. Dauber et al., *Phys. Rev. Lett.* **13**, 449–454 (1964). 3
- [10] A. Duane et al., *Phys. Rev. Lett.* **32**, 425–428 (1974). 3
- [11] G. W. London et al., *Phys. Rev.* **143**, 1034–1091 (1966). 3
- [12] T. Feldmann, P. Kroll, and B. Stech, *Phys. Rev.* **D58**, 114006 (1998). 3
- [13] P. Kroll. *Int. J. Mod. Phys.* **A20**, 331–340 (2005). 3
- [14] T. Huang and X.-G. Wu, *Eur. Phys. J.* **C50**, 771 (2007). 3, 5
- [15] M. Benayoun et al., *Phys. Rev.* **D59**, 114027 (1999). 3
- [16] S. D. Bass, *Phys. Lett.* **B463**, 286–292 (1999). 3
- [17] S. D. Bass, *Phys. Scripta* **T99**, 96–103 (2002). 3
- [18] P. Moskal, *Habilitation dissertation* Jagiellonian University, Cracow (2004).  
arXiv: hep-ph/0408162. 3, 11, 14, 18, 30
- [19] P. Moskal et al., *Phys. Rev.* **C79**, 015208 (2009). 3, 12, 18

- [20] A. Aloisio et al., *Phys. Lett.* **B541**, 45–51 (2002). 3, 52
- [21] R. Escribano and J. Nadal, *JHEP* **05**, 006 (2007). 3
- [22] F. Ambrosino et al., *Phys. Lett.* **B648**, 267–273 (2007). 3, 4, 52
- [23] H. Fritzsch and J. D. Jackson, *Phys. Lett.* **B66**, 365 (1977). 3, 5
- [24] J. Klaja, P. Moskal, and J. Zdebik, *Acta. Phys. Pol. Supp.* **B2**, 31–38 (2009). 3
- [25] B. Borasoy et al., *Phys. Lett.* **B643**, 41–45 (2006). 4, 52
- [26] M. J. Zieliński, *Diploma Thesis Jagiellonian University, Cracow* (2008). arXiv: hep-ex/0807.0576. 4, 52
- [27] A. Kupść et al., arXiv: nucl-ex/0803.2673 (2008). 4, 52
- [28] N. Beisert and B. Borasoy, *Nucl. Phys.* **A716**, 186–208 (2003). 4, 5
- [29] R. Nissler and B. Borasoy, *AIP Conf. Proc.* **950**, 188–191 (2007). 4, 5
- [30] M. Poppe, *Int. J. Mod. Phys.* **A1**, 545–668 (1986). 4
- [31] S. J. Brodsky and G. P. Lepage, *Phys. Rev.* **D24**, 1808 (1981). 4, 5
- [32] J. Z. Bai et al., *Phys. Lett.* **B594**, 47–53 (2004). 4
- [33] M. Acciarri et al., *Phys. Lett.* **B418**, 399–410 (1998). 5
- [34] K. Karch et al., *Z. Phys.* **C54**, 33–44 (1992). 5
- [35] D. Williams et al., *Phys. Rev.* **D38**, 1365 (1988). 5
- [36] G. P. Lepage and S. J. Brodsky, *Phys. Rev.* **D22**, 2157 (1980). 5
- [37] H. J. Behrend et al., *Z. Phys.* **C49**, 401–410 (1991). 5
- [38] B. Aubert et al., *Phys. Rev.* **D74**, 012002 (2006). 5
- [39] N. G. Deshpande and T. N. Truong, *Phys. Rev. Lett.* **41**, 1579 (1978). 5
- [40] P. Moskal et al., *Phys. Rev. Lett.* **80**, 3202–3205 (1998). 5, 18, 39
- [41] P. Moskal et al., *Phys. Lett.* **B474**, 416–422 (2000). 5
- [42] F. Hibou et al., *Phys. Lett.* **B438**, 41–46 (1998). 5
- [43] A. Khoukaz et al., *Eur. Phys. J.* **A20**, 345–350 (2004). 5

- [44] F. Balestra et al., *Phys. Lett.* **B491**, 29–35 (2000). 5
- [45] M. Aguilar-Benitez et al., *Phys. Rev. Lett.* **25**, 1635–1638 (1970). 5
- [46] T. A. Lasinski et al., *Rev. Mod. Phys.* **45**, S1–S175 (1973). 5
- [47] B. C. Maglich, *AIP Conf. Proc.* **717**, 37–48 (2004). 5, 6
- [48] H. Dombrowski et al., *Nucl. Phys.* **A626**, 427c–433c (1997). 8, 10
- [49] E. Czerwiński, *Diploma Thesis* Jagiellonian University, Cracow (2006). 8, 14, 18, 46
- [50] R. Maier, *Nucl. Instrum. Meth.* **A390**, 1–8 (1997). 8, 10
- [51] <http://www.fz-juelich.de/ikp/cosy>. 9
- [52] D. Prasuhn et al., *Nucl. Instrum. Meth.* **A441**, 167–174 (2000). 9, 10, 35
- [53] H. Stockhorst, *Schriften des FZ-Jülich, Matter and Materials* **11**, 176 (2002). 9, 10
- [54] S. Van Der Meer, *Rev. Mod. Phys.* **57**, 689–697 (1985). 10
- [55] H. Stockhorst et al., *FZ-Jülich, IKP Annual Report*, 160 (1997). 10
- [56] J. Marriner, *Nucl. Instrum. Meth.* **A532**, 11–18 (2004). 10
- [57] A. Täschner et al., *FZ-Jülich, IKP Annual Report*, 48 (2006). 11, 12
- [58] S. Brauksiepe et al., *Nucl. Instrum. Meth.* **A376**, 397–410 (1996). 12, 23
- [59] J. Smyrski et al., *Phys. Lett.* **B474**, 182–187 (2000). 12, 18
- [60] R. Czyzykiewicz, *PhD dissertation* Jagiellonian University, Cracow (2006). arXiv: nucl-ex/0702010. 12, 38
- [61] R. Czyzykiewicz et al., *Phys. Rev. Lett.* **98**, 122003 (2007). 12
- [62] J. Smyrski et al., *Nucl. Instrum. Meth.* **A541**, 574–582 (2005). 12
- [63] P. Moskal, *PhD dissertation* Jagiellonian University, Cracow (1998). 18, 43
- [64] P. Moskal et al., *Phys. Rev.* **C69**, 025203 (2004). 18
- [65] T. Sefzick, *FZ-Jülich, IKP Annual Report*, 14 (2002). 20
- [66] B. Gugulski, *Berichte des FZ Jülich KFA-IKP(I)-1992-3* (1992). 20

- 
- [67] P.A. Żołnierczuk, *PhD dissertation* Jagiellonian University, Cracow (1997). 20
- [68] T. Tanimori et al., *Nucl. Instrum. Meth.* **216**, 57–65 (1983). 23
- [69] P. Moskal et al., *Nucl. Instrum. Meth.* **A466**, 448–455 (2001). 29
- [70] D. Prasuhn, Private communication (2007). 29, 35, 38, 43
- [71] G. Schepers and D. Prasuhn, *FZ-Jülich, IKP Annual Report*, 47 (1996). 35
- [72] P. Moskal et al., *J. Phys.* **G32**, 629–641 (2006). 38, 39
- [73] J. Smyrski, *AIP Conf. Proc.* **950**, 146–149 (2007). 43
- [74] CERN Program Libraries Long Writeups W5013, (1994). 45
- [75] S. Baker and R.D. Cousins, *Nucl. Instrum. Meth.* **221**, 437–442 (1984). 45
- [76] G.J. Feldman and R.D. Cousins, *Phys. Rev.* **D57**, 3873–3889 (1998). 45
- [77] B. Kamys, Private communication (2009). 46, 51
- [78] J.P. Naisse et al., *Nucl. Phys.* **A278**, 506–524 (1977). 50
- [79] P. Moskal et al., *Phys. Lett.* **B482**, 356–362 (2000). 50
- [80] J. Przerwa, D. Grzonka, P. Klaja, P. Moskal, and W. Oelert, *Schriften des Forschungszentrums Jülich, Matter and Materials Band, Volume 36*, ISBN 978-3-89336-483-1 (2007). 52